Radar-Based Bayesian Estimation of Ice Crystal Growth Parameters within a Microphysical Model

ROBERT S. SCHROM,[a,b] MARCUS VAN LIER-WALQUI,[c,d] MATTHEW R. KUMJIAN,[e] JERRY Y. HARRINGTON,[e] ANDERS A. JENSEN,[f] AND YAO-SHENG CHEN[g]

[a] *NASA Goddard Space Flight Center, Greenbelt, Maryland*
[b] *Universities Space Research Association, Columbia, Maryland*
[c] *Center for Climate Systems Research, Columbia University, New York, New York*
[d] *NASA Goddard Institute for Space Studies, New York, New York*
[e] *Department of Atmospheric Science, The Pennsylvania State University, University Park, Pennsylvania*
[f] *National Center for Atmospheric Research, Boulder, Colorado*
[g] *Cooperative Institute for Research in Environmental Sciences, University of Colorado Boulder, Boulder, Colorado*

(Manuscript received 5 May 2020, in final form 10 October 2020)

ABSTRACT: The potential for polarimetric Doppler radar measurements to improve predictions of ice microphysical processes within an idealized model–observational framework is examined. In an effort to more rigorously constrain ice growth processes (e.g., vapor deposition) with observations of natural clouds, a novel framework is developed to compare simulated and observed radar measurements, coupling a bulk adaptive-habit model of vapor growth to a polarimetric radar forward model. Bayesian inference on key microphysical model parameters is then used, via a Markov chain Monte Carlo sampler, to estimate the probability distribution of the model parameters. The statistical formalism of this method allows for robust estimates of the optimal parameter values, along with (non-Gaussian) estimates of their uncertainty. To demonstrate this framework, observations from Department of Energy radars in the Arctic during a case of pristine ice precipitation are used to constrain vapor deposition parameters in the adaptive habit model. The resulting parameter probability distributions provide physically plausible changes in ice particle density and aspect ratio during growth. A lack of direct constraint on the number concentration produces a range of possible mean particle sizes, with the mean size inversely correlated to number concentration. Consistency is found between the estimated inherent growth ratio and independent laboratory measurements, increasing confidence in the parameter PDFs and demonstrating the effectiveness of the radar measurements in constraining the parameters. The combined Doppler and polarimetric observations produce the highest-confidence estimates of the parameter PDFs, with the Doppler measurements providing a stronger constraint for this case.

KEYWORDS: Cloud microphysics; Ice crystals; Radars/Radar observations; Bayesian methods; Cloud parameterizations

1. Introduction

Ice microphysical processes play a large role in governing the life cycles and macrophysical structure—and therefore the radiative properties—of many cloud systems. Unfortunately, our understanding of ice processes is still relatively crude, especially compared to our understanding of warm-cloud microphysics. As a result, significant uncertainties exist in the treatment of ice processes in models at all scales. The challenges in modeling cold clouds persist in part because of the myriad shapes ice crystals acquire during their lifetimes (e.g., Baker and Lawson 2006; Bailey and Hallett 2009), along with the complex interactions among these particles. Owing to the lack of theoretical understanding, modeling the evolution of particle shape, mass, and fall speed remains a significant challenge.

Recent modeling work has attempted to address this problem by allowing the bulk particle properties of ice hydrometeors (e.g., aspect ratio, density, and size) to evolve freely as continuous variables that depend on the environmental temperature and/or supersaturation (e.g., Chen and Lamb 1999; Hashino and Tripoli 2007; Harrington et al. 2013a,b; Morrison and Milbrandt 2015; Jensen and Harrington 2015; Chen and Tsai 2016; Jensen et al. 2017, hereafter J17). These "particle-property" approaches have a long history (e.g., Todd 1964; Hindman and Johnson 1972; Cotton 1972) and attempt to directly couple measured quantities to the evolution of hydrometeor properties. Many of these approaches have their roots in the work of Chen and Lamb (1994), where laboratory-measured axis growth rates inform the prediction of shape.

Although laboratory and in situ data are useful in constraining some aspects of how the ice particle properties evolve, these measurements have some important limitations. For example, large populations of interacting ice particles are difficult to generate in an idealized laboratory setting, and thus particles growing in the laboratory likely evolve differently compared to those in nature. Despite these limitations, laboratory experimentation and in situ observations are often used to critique model performance (Fridlind et al. 2007; Avramov and Harrington 2010, and many others); however, they are rarely used *in conjunction* with modeling studies to reduce the uncertainty and improve parameterizations of microphysical processes.

One set of measurements that provides additional constraints but has yet to be fully exploited is radar remote sensing. Radar remote sensing has been a popular choice to obtain a

Corresponding author: Robert S. Schrom, robert.s.schrom@nasa.gov

DOI: 10.1175/JAS-D-20-0134.1

qualitative understanding of ice growth processes (e.g., Kennedy and Rutledge 2011; Andrić et al. 2013; Kumjian et al. 2014; Schrom et al. 2015; Leinonen and Moisseev 2015; Oue et al. 2015b,a, 2016; Kneifel et al. 2015; Kumjian et al. 2016; Giangrande et al. 2016; Sinclair et al. 2016; Moisseev et al. 2017; Kumjian and Lombardo 2017; Vogel and Fabry 2018). The widespread usage of these measurements is partly because radar provides a more statistically robust sampling of hydrometeor properties than in situ observations, owing to its more comprehensive spatial coverage. However, the radar variables are complex, inherently uncertain functions of the ice properties predicted by microphysical models (e.g., Kumjian et al. 2019), necessitating the use of retrievals or forward operators to map between the model variables and radar variables. This mapping becomes necessary because the particle property assumptions used in the microphysical and forward models are often inconsistent. In addition, many assumptions about the particle properties—and, in turn, scattering properties—are built into the frameworks of such retrievals or forward operators (e.g., Ryzhkov et al. 2011); the validity of these ice particle property assumptions and their impact on uncertainties in the forward model or retrieval are often unexplored, precluding a quantitative application of radar measurements in evaluating microphysical models.

As such, particle-property modeling approaches, radar simulators, and observations have yet to be combined—with full consideration of the uncertainties inherent in each—to yield insights into poorly understood ice processes. However, recent improvements in radar forward models (e.g., Schrom and Kumjian 2019, hereafter SK19), novel usage of Bayesian parameter estimation techniques (e.g., Posselt and Vukicevic 2010; Morrison et al. 2020; van Lier-Walqui et al. 2020), and the increasing availability of multiparameter radar measurements collectively enhance the potential for radar measurements to *quantitatively* inform ice microphysical models. Specifically, Markov chain Monte Carlo (MCMC) samplers have shown promising results in informing microphysical processes with radar observations (e.g., van Lier-Walqui et al. 2012). This method is ideally suited to constrain the parameters associated with ice particle growth and to characterize their error structures, even in the presence of highly nonlinear sensitivities of the model to perturbations of these parameters (Posselt and Vukicevic 2010).

The purpose of the effort described herein is twofold: first, we demonstrate the utility of MCMC in estimating the uncertain parameters in an ice particle growth model, informed by polarimetric and Doppler radar observations. Given the relative novelty of our approach, we avoid combinations of growth processes (i.e., vapor growth, riming, and aggregation) and focus solely on constraining simulations of vapor-grown planar ice crystals in an observed Arctic mixed-phase cloud (combined growth processes will be discussed in a future study). Second, we explore the relations among the MCMC-derived parameters governing the ice crystal shape, those governing the model kinematic and thermodynamic environment, and the radar measurements. We also develop a method to incorporate various crystal structures into the modeled ice effective density, a variable that strongly impacts the model uncertainty.

The microphysical model for vapor deposition and the kinematic model framework are described in section 2, along with a description of the new parameterization of ice effective density. Section 3 describes the observations associated with the Arctic vapor deposition case and describes the parameter estimation technique. The results are presented in section 4, followed by a discussion and summary in section 5.

2. Microphysical and kinematic models

a. Microphysical model

We use the Ice-Spheroids Habit Model with Aspect-Ratio Evolution (ISHMAEL; J17). ISHMAEL has been used to explore mixed-phase stratocumulus formation (Simpfendoerfer et al. 2019) and dissipation (Sulia et al. 2014), a quasi-idealized 3D squall line (Jensen et al. 2018b), and orographic precipitation from the IMPROVE-2 campaign (Jensen et al. 2018a). Following Chen and Lamb (1994), ice particles are represented by spheroids with the major and minor dimensions referenced to the semiaxis lengths of the basal (a) and prism (c) faces, respectively, of an ice crystal. This approach provides a mechanism to change the aspect ratio ($\phi = c/a$) of the modeled crystals, as well as their effective density (ρ_{eff}). The ability of this model to freely evolve ice crystal ϕ, maximum size, and ρ_{eff} is well suited for the purpose of simulating polarimetric radar measurements of branched planar crystals, which depend on the same quantities (e.g., SK19). As in Harrington et al. (2013a), we represent the particle size spectra using Gamma distributions within a bulk parameterization for the evolution of the particle properties during growth—in this study, the shape parameter is fixed, with the total number and slope parameters evolving according to the growth equations. We fix the shape parameter for the purposes of simplicity; since the shape parameter tends to have a larger impact on the smallest sizes in the particle spectrum, the reflectivity-weighted observations used herein are less sensitive to the shape parameter, and therefore likely provide minimal information needed to constrain this parameter.

To evolve shape during vapor growth, the model incorporates the mass distribution hypothesis of Chen and Lamb (1994),

$$\frac{dc}{da} = \frac{\alpha_c}{\alpha_a}\frac{c}{a} \equiv \Gamma\frac{c}{a}, \tag{1}$$

where α_c and α_a are the deposition coefficients for the a and c axes of the crystal, respectively, and Γ is the inherent growth ratio. The deposition coefficients (and thus Γ) account for all surface processes that influence the incorporation of water molecules into the bulk crystalline lattice. They can be thought of as growth efficiencies with values between zero and unity, and thus describe the overall mass uptake and the evolution of particle shape (Lamb and Scott 1974; Libbrecht 2003). The Γ has a known temperature (T) dependence at liquid saturation that can be directly quantified from laboratory data (Lamb and Scott 1974) or predicted based on laboratory-determined critical supersaturations

(Nelson and Baker 1996; Zhang and Harrington 2014; Harrington et al. 2019). Thus, Γ governs particle ϕ evolution, allowing the development of planar (oblate) or columnar (prolate) particles over time. However, laboratory measurements of Γ indicate a wide range of values for a given temperature (as much as a factor of 2; see Fig. 3 in Chen and Lamb 1994). Therefore, it is a source of uncertainty in simulations of vapor growth.

The initiation of ice crystals requires a nucleation mechanism; however, the ice nuclei concentrations for the simulated case are unknown. Instead of using an explicit ice nucleation scheme, we employ the method of Ovchinnikov et al. (2014), where a target ice number concentration N_{ice} is replenished if the ice crystal population is depleted below N_{ice}, conditional on supersaturation with respect to ice $s_i \geq 5\%$. By sampling different values of N_{ice}, we attempt to constrain its value and determine its relations to the other microphysical parameters within our parameter estimation framework.

Supercooled liquid water is represented here as in J17, where it is assumed to follow a Gamma distribution. However, the liquid water simulated for this case is minimal, with simulated liquid water path (LWP) values on the order of those observed during this case ($\leq 20\,\text{g m}^{-2}$; Oue et al. 2016); in situ photographs of the observed particles also appear unrimed during this case. Because these liquid drops have negligible impact on the radar variables, and riming was minimal during this case, the treatment of the liquid phase herein has little on impact the parameter estimation results.

b. Size-dependent deposition density parameterization

Another uncertainty in ISHMAEL is the assumed structure, or secondary habit characteristics (e.g., placement and dimensions of branches and subbranches, hollowing), of growing ice crystals. All microphysical models implicitly or explicitly parameterize these secondary habit structures with a ρ_{eff} that corresponds to the mass of the structures divided by the particle volume; this particle volume is typically assumed to be that of a sphere or spheroid (e.g., Brown and Francis 1995; Heymsfield et al. 2004). We assume the particle volume herein to be that of the smallest hexagonal prism that encloses the crystal. In doing so, the scattering properties are most closely related to the ice crystal structure [as in Schrom and Kumjian (2018) and SK19]. In contrast, using a spherical bounding volume to characterize the effective density of thin planar crystals will enclose an artificially large region of air, substantially reducing the effective density and resulting in severe underestimates of the near-field interactions responsible for the polarimetric scattering properties (Schrom and Kumjian 2018).

The model of J17 calculates ρ_{eff} by assuming that mass added during a short interval of vapor deposition has a "deposition density" (ρ_{dep}) that represents the mixture of air and ice associated with an assumed secondary habit structure, where $\rho_{\text{dep}} \leq$ the density of ice $\rho_i = 920\,\text{kg m}^{-3}$. Thus, the change in particle volume is determined by ρ_{dep}. ρ_{dep} is often parameterized as a function of T and s_i based on laboratory measurements (Chen and Lamb 1994). The parameterization is generally applied once a crystal grows beyond some core semiaxis size of a_c,

$$\rho_{\text{dep}}(a) = \begin{cases} \rho_i, & \text{if} \quad a \leq a_c \\ \rho_{\text{dep}}(T, s_i), & \text{if} \quad a > a_c. \end{cases} \tag{2}$$

Though this approximation for ρ_{dep} was never meant to capture the true structure of branched crystals, it inherently assumes a crystal structure with a solid-ice core of semiaxis length a_c and a coverage of branches and subbranches that is fixed in size during growth for $a > a_c$; these assumptions naturally lead to a ρ_{eff} that rapidly approaches ρ_{dep} (see below).

Improvements to this approach are possible, and should align with the observational evidence of planar crystals growing at temperatures near −15°C (e.g., Nelson 2005; Takahashi 2014), showing that ρ_{dep} varies with size. Additionally, a variety of structures are possible at these temperatures, including more fern-like dendrites, broad-branched sector plates, and thin-branched stellar crystals (e.g., Magono and Lee 1966; Bailey and Hallett 2009; Takahashi 2014). Hereafter, these ice crystal forms are collectively referred to as "branched planar crystals." Predicting these structures based on the ambient T and s_i is not possible with current theory, and may be fundamentally limited to a certain degree of natural variability given randomness of ice crystal defects, ice nuclei properties, etc. (e.g., Libbrecht 2005). However, capturing the variability in these structural features is desirable because of the significant impact the ice structure has on its electromagnetic scattering properties (SK19).

To improve the estimation of ice structure, we adapt the synthetic branched planar structure generation method from SK19[1] for the purpose of developing an analytical, size-dependent ρ_{dep} model, given in the appendix. An attractive feature of this structure generation method is that it depends on several physically identifiable quantities that can readily be implemented in a microphysical modeling framework. Additionally, for a given set of these quantities, we can determine both an analytical ρ_{dep} function with respect to the crystal size and the corresponding evolution of "real" structures that may, at least qualitatively, be evaluated using images of ice crystals from the event (e.g., Oue et al. 2016). However, rather than performing scattering computations for these structures directly, we use the bulk physical properties (e.g., ϕ, ρ_{eff}, and size) simulated by the microphysical model as inputs to the analytical SK19 radar forward model, allowing for the uncertainty in scattering properties given a set of simulated bulk physical properties to be incorporated into the Bayesian parameter estimation method. The fact that the same assumed shapes were used in the development of the SK19 radar forward model ensures that the simulated scattering and physical properties within our framework are consistent, and thus provides for a more robust estimation of assumed shape parameters.

The differences between the size-dependent- and fixed-ρ_{dep} models can produce large differences in the crystals' electromagnetic scattering properties during growth. We demonstrate

[1] The method in that study was used to calculate scattering properties of semirealistic crystals; analytical fits of these scattering properties to the physical properties of ϕ, ρ_{eff}, and size were then used to develop the radar forward model that we adopt herein.

this by comparing the differential reflectivity Z_{DR} predicted using both ρ_{dep} functions for single-particle growth coupled to the branched planar crystal forward model of SK19. We artificially evolve ϕ as a function of size for a single branched planar crystal using the ϕ–size power law relation of SK19, with exponent $b = 0.5$ and a growing from 0.01 to 3 mm. For the fixed-ρ_{dep} model, we set $\rho_{dep} = 250\,\text{kg m}^{-3}$ and $a_c = 0.1$ mm; for the size-dependent ρ_{dep} model we use the same a_c and values of $f_b = 0.4$, $f_i = 0.5$, and $f_t = 0.3$ (defined in the appendix). We choose these parameters to demonstrate a different structure evolution that has a similar ρ_{eff} at its maximum size as that for the fixed-ρ_{dep} model. ρ_{dep} and ρ_{eff} for these two models are shown in Fig. 1. The fixed-ρ_{dep} model produces a ρ_{eff} that decreases rapidly from solid ice to the fixed ρ_{dep} value as a grows beyond a_c. In contrast, the size-dependent-ρ_{dep} parameterization decreases at a slower rate with a.

With respect to the scattering properties, both models have rapidly increasing Z_{DR} up to ~7.3 dB during the early stages of vapor growth where $a < a_c$ (Fig. 2, lower right). Once $a > a_i$, the fixed-ρ_{dep} model features rapid decreases in ρ_{eff}, and Z_{DR} decreases to a minimum value of ~4 dB, before increasing to ~6 dB at $a = a_{max}$. For the size-dependent ρ_{dep}, Z_{DR} decreases gradually to a local minimum of ~6.3 dB near $a = 0.5$ mm. As a increases further, the Z_{DR} reaches another local maximum of ~6.6 dB before decreasing to ~6 dB at $a = a_{max}$ (Fig. 2, upper left).

These two distinct Z_{DR} behaviors are a consequence of the unique ρ_{eff} curves at different stages of growth; despite both particles eventually reaching similar ϕ and ρ_{eff} (and thus similar Z_{DR}), they approach these values through vastly different paths in the ϕ–ρ_{eff} particle-property space, further illustrating the impact of the assumed crystal structure in interpreting vertical profiles of radar measurements. The growth pathway associated with the size-dependent ρ_{dep} model is consistent with observations (e.g., Oue et al. 2016) and scattering calculations (e.g., Lu et al. 2016; SK19) and is based on more realistic ice crystal shapes. Thus, we incorporate this ρ_{dep} formulation into the microphysical model component of our framework to better explore the variability of ice crystal structures that are consistent with the radar observations.

To verify that this new ρ_{dep} formulation is also consistent with laboratory measurements, we perform time series simulations of crystal ϕ with this formulation and compare them with the wind tunnel measurements of Fukuta and Takahashi (1999). Figure 3 shows the a and c axes of dendritic crystals grown at liquid saturation, −15°C, and as a function of time. The crystals were modeled using the ρ_{dep} proposed by Chen and Lamb (1994) and the function proposed here. Because the initial crystal size was not precisely known in the measurements, a range of initial sizes ($a = 1$ to 10 μm) were used. The results show that both ρ_{dep} formulations can reproduce the evolution of the axis lengths. Note that the particle must reach 100 μm across before the Chen and Lamb (1994) density function is used, otherwise its ϕ becomes too extreme. The function proposed in this work produces a more realistic decrease in density with time (Fig. 3, right panel), and one that also produces realistic scattering behavior (see above), unlike the density function of Chen and Lamb (1994).

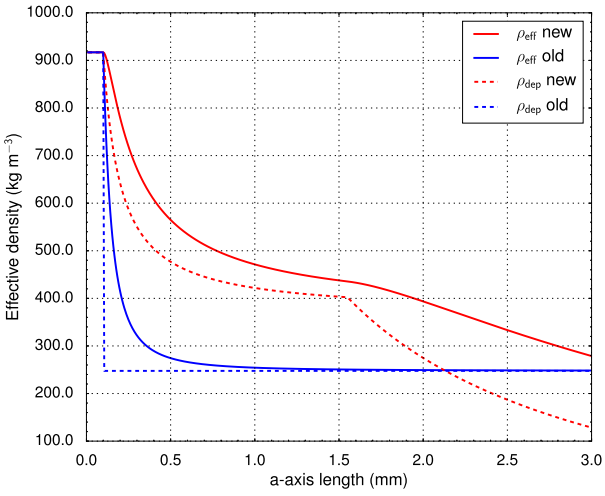

FIG. 1. Plot of deposition density (dashed lines) and effective density (solid lines) for a crystal at sizes from $a = 0.01$ to $a = 3.0$ using the deposition density model developed herein (red) and the deposition density model of Jensen and Harrington (2015), with $a_c = 0.1$ mm and $\rho_{dep} \approx 250\,\text{kg m}^{-3}$ (blue). The crystal structure quantities for the deposition density shown here are $a_c = 0.1$ mm, $f_b = 0.4$, $f_i = 0.5$, and $f_t = 0.3$.

c. *Kinematic model*

We incorporate the modifications to the microphysical model for vapor growth described above into the Eulerian two-dimensional (2D) kinematic framework (Szumowski et al. 1998) used in prior work (Sulia et al. 2013; J17). This framework has a prescribed flow field such that there are no feedbacks between the microphysics and the dynamics. We can thus more directly perturb the microphysical growth conditions and better understand their impact on the radar variables. Also, this approach allows us to more efficiently perform the large number of simulations required for robust sampling with MCMC, compared to more resource-intensive dynamical models.

The kinematic model uses a streamfunction formulation for the wind field (e.g., Grabowski 1998). The horizontal component of the streamfunction varies sinusoidally so that two updraft/downdraft cells are present, whereas the vertical component varies as a Gaussian. To focus only on sensitivities to the vertical velocity profile, we perturb the streamfunction amplitude (C_{w_s}; related to the velocity magnitude), the Gaussian standard deviation (C_{d_s}; corresponding to the updraft depth), and the Gaussian centroid (C_{Z_0}; corresponding to the height of the maximum vertical velocity).

Unavoidably, there is representation error (e.g., Janjić and Cohn 2006; Hodyss and Nichols 2015) associated with the fact that the 2D model does not represent the true (3D, evolving) dynamical processes captured in the radar observations of the natural cloud system. We mitigate these errors by including C_{w_s}, C_{d_s}, and C_{Z_0} in the set of unknown parameters. Because all components of this expanded parameter vector are perturbed simultaneously, correlation in uncertainty between kinematic and microphysical parameters can indicate where errors associated with uncertainty in the kinematic framework

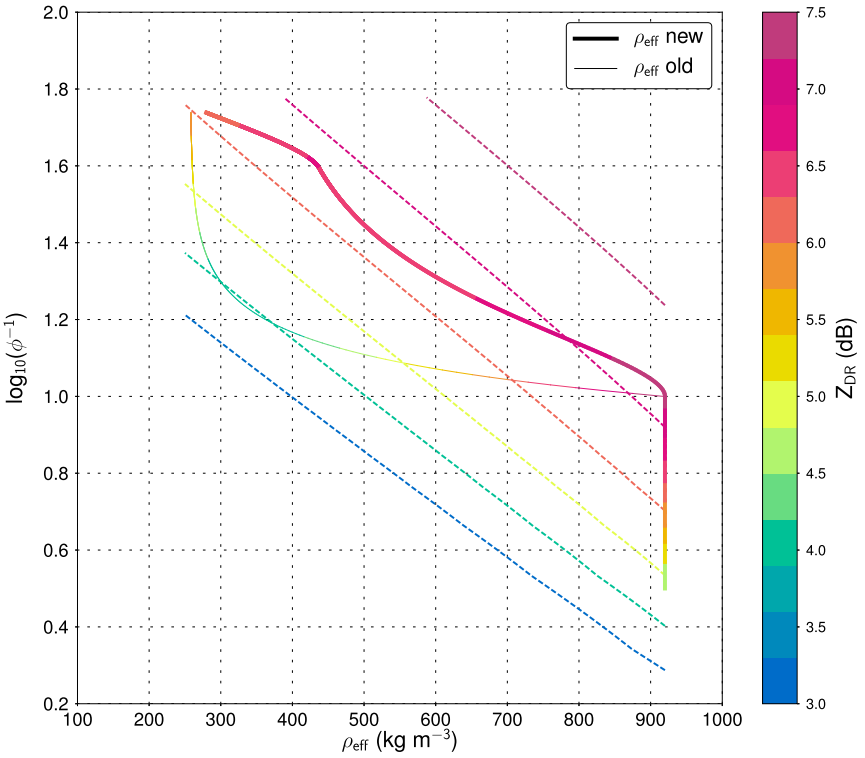

FIG. 2. Plot of ρ_{eff} and ϕ evolution (using the power-law relation described in the text) for particles growing from 0.01 to 3 mm (solid lines; the color indicates the corresponding value of single-particle Z_{DR} simulated using the forward model from SK19). The thin line indicates the particle growing with a deposition density from Jensen and Harrington (2015) with $\rho_{dep} \approx 250\,kg\,m^{-3}$ and $a_c = 0.1$ mm. The thick line indicates the particle growing with the new deposition density model developed herein, with $a_c = 0.1$ mm, $f_b = 0.4$, $f_i = 0.5$, and $f_t = 0.3$. The dashed contours indicate values of Z_{DR} as functions of $\log_{10}(\phi^{-1})$ and ρ_{eff} from the forward model and are plotted in increments of 1 dB.

impact the best-performing values of microphysical parameters. By identifying any potential compensating errors, these results will give insight into the degree to which modeling assumptions affect estimation of microphysical parameters.

An example of the 2D wind field used herein is shown in Fig. 4. The initial T and moisture profiles are based on an observed sounding at 1730 UTC from the case described below. The model is then run out to a simulation time of 90 min with a time step of 1 s. The horizontal and vertical grid spacings are 80 and 40 m, respectively, and the domain extends 3 km in the vertical and 1.6 km in the horizontal. Advection is calculated using the multidimensional positive definite advection transport algorithm (MPDATA; Smolarkiewicz 1984; Smolarkiewicz and Margolin 1998); this scheme captures the evolution of particle properties on the Eulerian grid from the combined effects of vapor growth, sedimentation, and transport from the wind field.

3. Experimental design

a. *Case study—2 May 2013, Utqiaġvik, Alaska*

On 2 May 2013, ice-phase precipitation from a stratiform, mixed-phase cloud was observed at the Department of Energy Atmospheric Radiation Measurement (ARM; Mather and Voyles 2013) research site at Utqiaġvik (formerly known as Barrow), along the North Slope of Alaska. This case is described in detail by Oue et al. (2016). The precipitation was observed by several ARM instruments at the site, including the X-band Scanning Precipitation Radar (X-SAPR) and the Ka-band ARM Zenith-Pointing Radar (KAZR). The X-SAPR operates at 9.6 GHz with simultaneous transmission of horizontally and vertically polarized radiation. During the 2 May case, X-SAPR performed surveillance [plan position indicator (PPI)] scans and hemispheric range–height indicator (HRHI) scans, providing fields of equivalent radar reflectivity factor at horizontal polarization (Z), mean Doppler velocity (MDV), Doppler spectral width (σ_v), and the dual-polarization radar variables of differential reflectivity (Z_{DR}), differential phase shift (Φ_{dp}), and copolar cross-correlation coefficient (ρ_{hv}); owing to the limited information content of (ρ_{hv} for this case and the relatively poor quality of the X-SAPR Φ_{dp} field (Oue et al. 2016), we only use the Z and Z_{DR} measurements from this radar. See Kumjian (2013a,b,c) for a review of the polarimetric radar variables. The KAZR transmits microwave radiation at 35 GHz, and receives the co and cross-polar components of the scattered signal. This provides measures of equivalent radar

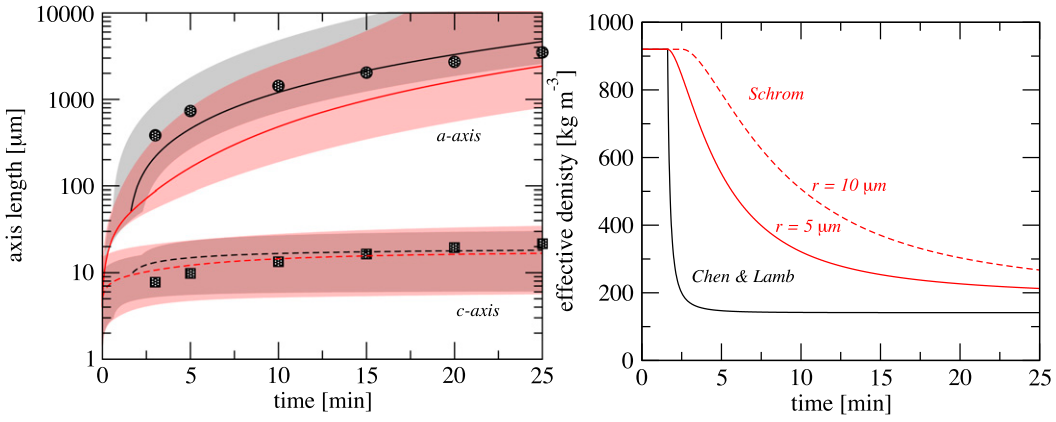

FIG. 3. Particle *a*- and *c*-axis lengths as a function of time for dendrites grown in a wind tunnel at liquid saturation and at −15°C (black solid circles; Fukuta and Takahashi 1999). Simulated *a*- and *c*-axis lengths are shown with the solid and dashed lines, respectively. The black curves use the deposition density from Chen and Lamb (1994) whereas the red curves use the deposition densities from Fig. 1 above and an initial particle radius of 5 μm. The black and red shaded regions show the range of solutions for initial particle radius from 1 to 10 μm. (left) The effective particle density as a function of time for Chen and Lamb (1994) (black lines) and using our density functions (red lines) with two initial radii shown. The parameters we use here for our deposition density function are $a_c = 0.01$, $f_b = 0.2$, $f_i = 0.2$, and $f_t = 0.2$.

reflectivity factor Z, linear depolarization ratio (LDR), and MDV (for zenith-pointing radars, MDV is the reflectivity-weighted mean of the particles' vertical motion). Owing to the lack of sensitivity in LDR for KAZR (minimum detectable value of −21 dB; Oue et al. 2015b) and the minimal expected LDR values for planar crystals (e.g., Tang and Aydin 1995), we use only Z and MDV from this radar. Together, these measurements provide bulk information about the ice particle sizes, shapes, and fall speeds, important microphysical quantities that are all represented within ISHMAEL.

Following Oue et al. (2016), the X-SAPR data are averaged over a region bounded by the boxes in Fig. 5, whereas the KAZR measurements are averaged in time (between 1545 and 1620 UTC as indicated in Fig. 6); the X-SAPR averaging region

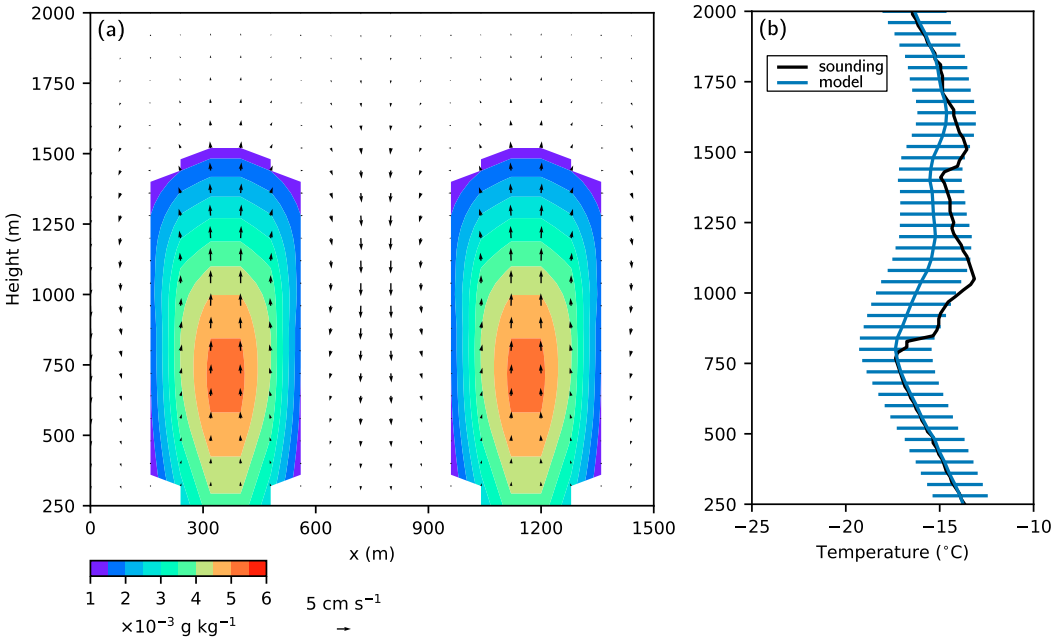

FIG. 4. Plot of (a) mean wind vectors and mean ice mass mixing ratio (shaded contours) and (b) simulated mean temperature profiles (blue; observed sounding from 1730 UTC in black), with bars indicating the 1σ ranges from 100 simulations using unique samples of the parameters drawn from the posterior MCMC distribution. The temperature profiles correspond to vertical profiles at $x = 320$ m.

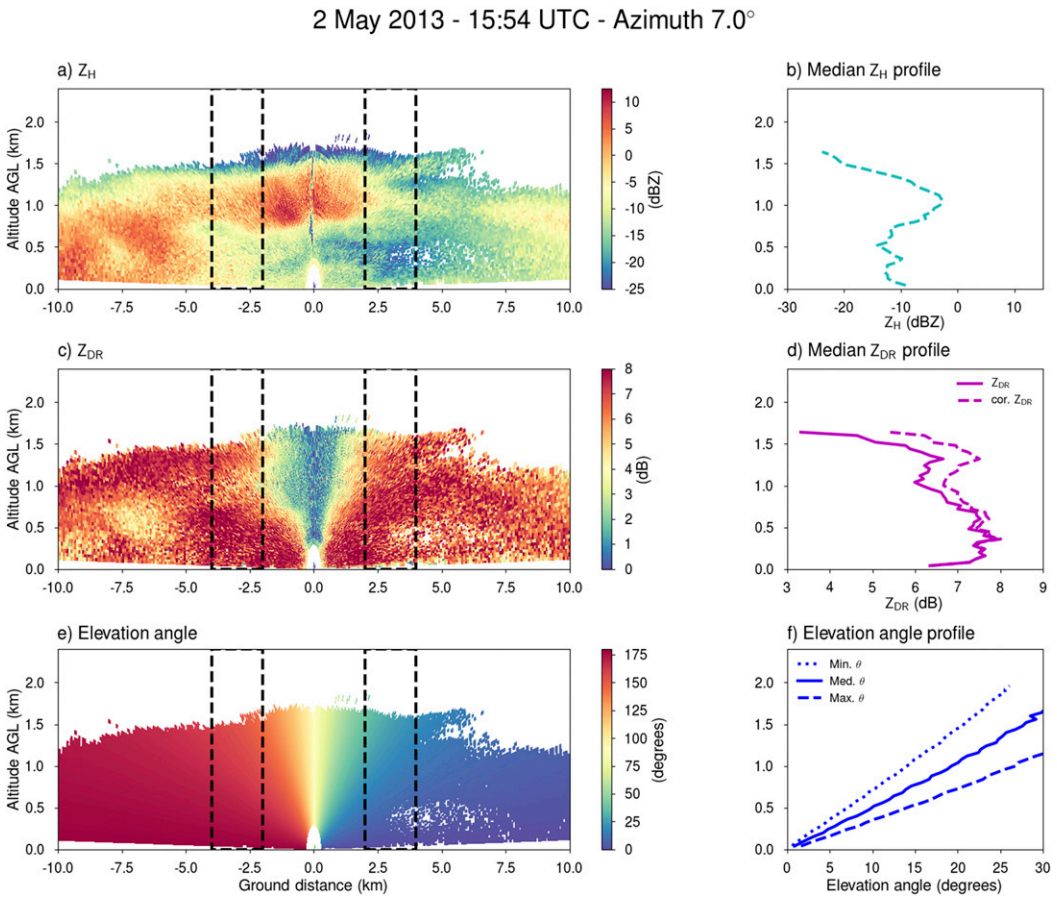

FIG. 5. The 7°-azimuth HRHI observations of (a) Z, (c) Z_{DR}, and (e) the corresponding elevation angles from the X-SAPR radar at the ARM NSA site at 1554 UTC 2 May 2013. The median profiles are for (b) Z, (d) Z_{DR}, and (f) elevation angle, where the values are binned within the observational domains indicated by the black outlines in the HRHI panels at each height. The profile in (d) includes the median Z_{DR} (solid line) and the corrected median Z_{DR} (dashed line) based on the median elevation angle at each height. Specifically, the median Z_{DR} is divided by the cosine squared of the median elevation angle at each height. The bounds of the elevation angles at each height within the observational domains are shown plotted as the dashed lines in (f).

is chosen to be >2 km from the radar to ensure that the elevation angles are <30°. These data are binned in 40-m height increments, with the mean and standard deviation of each radar variable calculated within each height bin to obtain the vertical profiles. Thus, the averaging involves data from different sampling volumes at different times. Nevertheless, the averaged Z (shown in Fig. 7) illustrates the consistency between the two sets of radar data, with differences < 5 dB at heights > 1 km despite the large vertical gradients in Z (>25 dB km^{-1}). From a forward modeling perspective, the wavelength and incidence angle differences (X-SAPR: X band, side incidence; KAZR: Ka band, vertical incidence) for the vast majority of branched planar ice crystals produced by the model result in minimal differences in Z (<0.5 dB) and thus can be considered comparable (Fig. 8; subject to the caveat that the averaging regions mentioned above are different). Given our simplified kinematic modeling framework, the goal here is not to reproduce this particular case, but rather to use observations consistent with pure vapor depositional growth to inform the uncertain microphysical model parameters in the highly idealized framework as a proof of concept.

With respect to the average vertical profiles of the radar variables, Z generally increases toward the ground, indicative of increased particle sizes and/or concentrations (Fig. 7). The growth is especially pronounced from ~1.7 to ~1.3 km AGL. Z continues to increase until about 1 km AGL, where it starts to decrease toward the ground. The Z_{DR} profile shows rather large values (>6 dB) throughout this layer,[2] indicating highly nonspherical, horizontally oriented particles, with relatively minimal changes in Z_{DR} with height. Such high Z_{DR} values are atypical of midlatitude precipitation systems

[2] Because of X-SAPR's limited sensitivity, Z_{DR} measurements are not available above about 1500 m AGL. See Oue et al. (2016) for details.

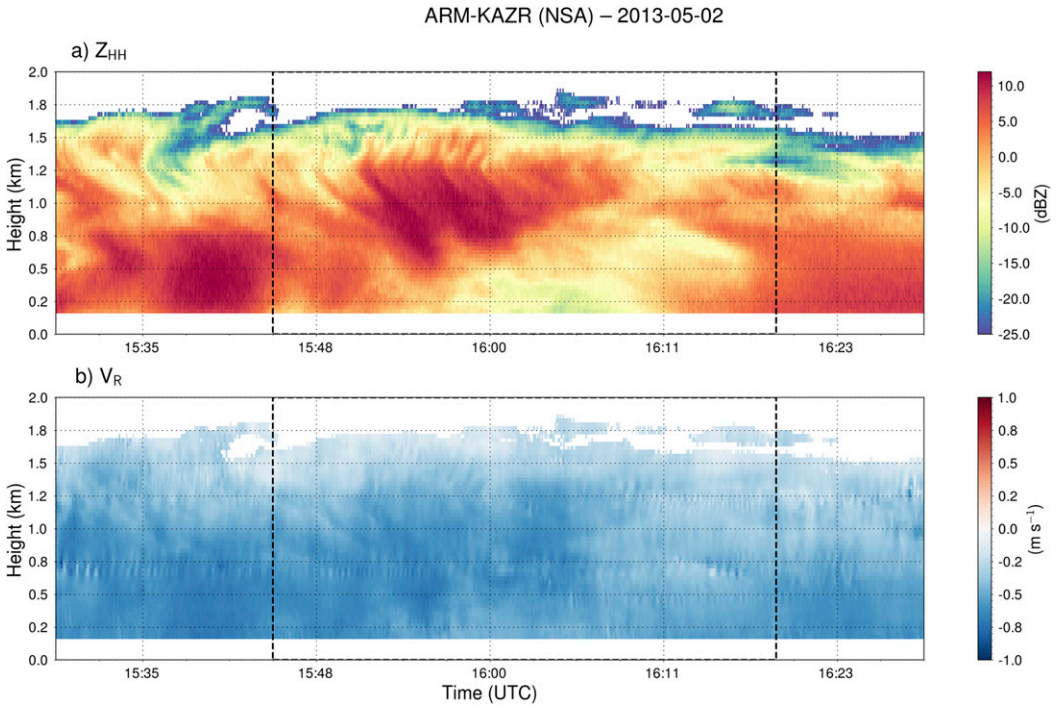

FIG. 6. KAZR time–height observations of (a) Z and (b) MDV between 1530 and 1630 UTC at the ARM NSA site on 2 May 2013. The dashed black outline indicates the averaging region for the mean profiles shown in Fig. 7.

(e.g., Schrom et al. 2015; Schrom and Kumjian 2016; Kumjian and Lombardo 2017) and suggest pristine ice crystals with very little ongoing aggregation or riming. Relatively low liquid water paths (LWP) of ~10–20 g m^{-2} (derived from 23.8- and 31.4-GHz ARM microwave radiometer measurements; Gaustad et al. 2011) were also observed during this case (Oue et al. 2016), providing additional evidence that growth by riming was minimal. However, these LWP values are somewhat unreliable given that they are within the 5–30 g m^{-2} range of uncertainty of the LWP retrieval (Liljegren et al. 2001). Additionally, some riming is possible within low-LWP environments (e.g., Moisseev et al. 2017), increasing ρ_{eff} and leading to a potential mischaracterization of these lightly rimed particles as higher-density branched planar crystals.

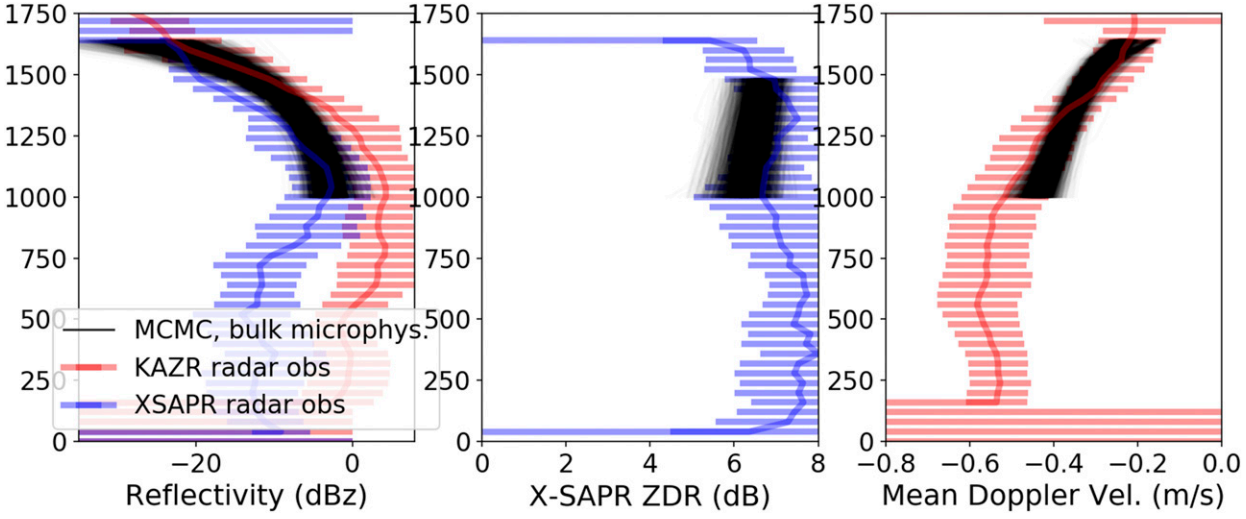

FIG. 7. KAZR observations (red, with 1σ errors), X-SAPR observations (blue, with 1σ errors) and forward-simulated observations (black) drawn from posterior distribution of model solutions.

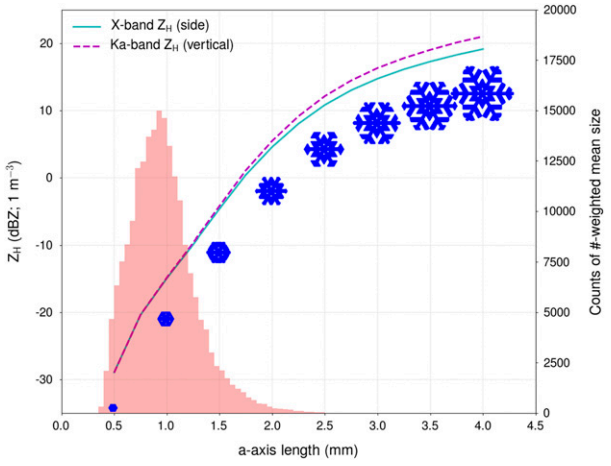

FIG. 8. Comparison of Z given 1 m^{-3} crystals growing from $a = 0.5$ mm to $a = 4.0$ mm for X band at side incidence (solid cyan line; corresponding to X-SAPR) and Ka band at vertical incidence (dashed magenta line; corresponding to KAZR). The 2D ice crystal structures used in the Amsterdam discrete dipole approximation (ADDA; Yurkin and Hoekstra 2011) calculations are plotted in blue. An overlay of the histogram of number-weighted mean a-axis lengths from the MCMC simulations is plotted in red.

KAZR MDV profiles show increasingly negative values (i.e., particle motion toward the radar) between −0.4 and −0.6 m s^{-1} in this layer, suggesting increased fall speeds as particles grow by vapor diffusion (Fig. 7). Because the observations suggest most vapor growth occurs above 1 km, we focus on this region in our simulations.

b. MCMC parameter estimation

We use a MCMC-like algorithm, the adaptive Metropolis sampler (Haario et al. 2001), constrained by the radar observations described above, to perform parameter estimation within the kinematic model framework. This modeling framework consists of the static kinematic flow field, the microphysical model equations driven by the flow field and thermodynamic environment, and the polarimetric radar forward model of SK19. Observations are drawn from the horizontal column at $x = 320$ m within the 2D kinematic field shown in Fig. 4. The choice of location of this column introduces some uncertainty; this location produces profiles closest to the observations, and therefore represents an observationally justified best choice given the idealized nature of the model framework. The observational uncertainties are assumed to be the sum of Gaussian variances from instrument uncertainty and forward-simulator uncertainties; the latter are described in SK19. Instrument uncertainties may be produced by noise or calibration errors, but in this case we consider the primary source to be uncertainty associated with averaging in space (for the X-SAPR) or in time (for the KAZR). The uncertainties are shown in Fig. 7 as the standard deviation of variability in the averaging window. We assume no correlation between sources of uncertainty.

The MCMC algorithm estimates the solution to Bayes's theorem, the posterior probability density function $P(\mathbf{x}|\mathbf{y}, M)$—the probability of parameters $\mathbf{x}$ given observations $\mathbf{y}$ and model M (van Lier-Walqui et al. 2020, and references therein). The uncertain parameters included in the MCMC sampling are those associated with the assumed branched planar crystal structures (f_b, f_i, f_t, and a_c; defined in the appendix), the target ice crystal concentration (N_{ice}), a multiplicative factor on the inherent growth ratio (C_{IGR}), and the multiplicative factors governing the kinematic model flow field (C_{d_s}, C_{w_s}, and C_{Z_0}). In this way, the MCMC algorithm simultaneously estimates parameters that directly impact the simulated radar variables via perturbations of the vapor depositional growth parameterization and the kinematic field. Besides the constraint offered by radar observations, we also include the restriction that particle density not exceed 750 kg m^{-3}—parameter values that produce particle density outside this range are given posterior probability of zero. We use this threshold essentially as an additional observational constraint based on observed photographs of branched planar crystals from Oue et al. (2016); only highly compact sector plates and solid-ice plates are able to achieve these high effective densities for planar crystals. Additionally, our MCMC results shown below indicate rapidly decreasing probability densities for effective densities 550 kg m^{-3}, indicating that this threshold has minimal impact on the results.

We also account for an additional uncertainty in the characteristic size used to determine the value of ρ_{dep} during growth. As for the other elements of the microphysical growth processes, this characteristic size is necessary to incorporate the new ρ_{dep} formulation into the bulk model (e.g., Harrington et al. 2013a), where the value of ρ_{dep} at the characteristic size is used in the growth equations for the entire size spectrum (ρ_{eff} is therefore also fixed over the spectrum). In particular, the characteristic size is the number-weighted mean size divided by the size distribution shape factor ($\nu = 4$; see Harrington et al. 2013a). Therefore, we must scale the critical sizes a_c and $a_{\max}$ such that this characteristic size corresponds to a representative size for the ρ_{dep} of the size spectra; naïvely using the characteristic size with a fixed $a_{\max} =$ mm will result in nearly all solid-ice plates. Therefore, we scale a_c and $a_{\max}$ by a heuristic factor 0.2 such that the density simulated by the model more accurately reflects that of the natural branched planar crystals that dominate the radar backscatter. To account for the uncertainty in this scaling factor, we apply an additional multiplicative adjustment factor C_a to further scale both a_c and $a_{\max}$, and include it as an additional parameter to perturb within the MCMC algorithm.

In reality, the crystal structure parameters f_b, f_i, f_t, and a_c likely depend on T, s_i, and initial size, and thus may have preferred values corresponding to the ambient in-cloud conditions. However, a single fixed value of each is held constant for each simulation (as selected by the MCMC sampling algorithm). The particle growth depends on these parameters, as well as the spatially varying environmental conditions, and thus these parameters will produce unique spectra of planar crystals with associated particle properties. Although somewhat unphysical, we apply this "naïve" approach to explore how much information the radar may provide as constraint. Because the growth pathway of the ice crystals exclusively

TABLE 1. Description of the parameters and the ranges of their values (inclusive) used to perturb the model simulations.

Quantity	Description	Minimum value	Maximum value	Sampling scale
C_{IGR}	Inherent growth ratio scaling	0.2	6.0	Linear
a_c	Core a-axis side length	1 μm	200 μm	Linear
f_b	Subbranch fractional area coverage	0.01	0.8	Linear
f_t	Tip width fraction	0.2	1.0	Linear
f_i	Inscribed hexagon fractional distance	0.1	1.0	Linear
C_{w_s}	Updraft velocity magnitude scaling	0.5	5.0	Linear
C_{d_s}	Updraft depth scaling	0.5	4.0	Linear
N_{ice}	Target ice concentration	$0.001\,\mathrm{L}^{-1}$	$1.78\,\mathrm{L}^{-1}$	$\log_{10}$
C_{Z_0}	Updraft central height scaling	0.0	1.0	Linear
C_a	Representative a-axis length scaling	0.2	1.0	Linear

involves nucleation aloft and growth with sedimentation through a relatively narrow range of environmental conditions (cf. Fig. 4), the sampled ice structure parameters can be thought of as corresponding to the integrated Lagrangian growth history of the particles. In that sense, the crystal structure parameters correspond to an average growth history of the particles over their trajectories, and should be so considered in the interpretation of the results. Given that we consider only Z, Z_{DR}, and MDV herein, mixtures of branched planar crystals with a variety of shape evolutions can be effectively represented by a single representative shape evolution that corresponds to the averaged Lagrangian growth history of the particles.

The prior distributions for parameters are chosen to be uniform with wide bounds, reflecting the general lack of available prior knowledge. For some of the parameters (f_t, f_i, f_b, and C_{Z_0}), there are explicit physical bounds that define the endpoints of the prior distributions, and we set the prior distributions for these parameters to sample between these endpoints. In other cases (C_{IGR}, C_{w_s}, C_{d_s}, C_a, a_c, and N_{ice}), the prior parameter ranges are chosen to be wide ranges over an initial set of parameter values that produced relatively close comparisons with the radar observations; this initial set of parameter values was determined based on tests on a number of individually run simulations. With respect to the prior bounds on these parameters, unrealistic model simulations for certain parameters provided additional information on the parameter ranges. For example, selecting C_{d_s} above a certain value can produce unrealistic vertical motion (relative to the maximum value in the profile) at the surface. Additionally, these parameters are chosen to be uncorrelated in the prior distribution, with the MCMC algorithm itself producing the posterior parameter PDF that can reveal such relations between parameters. The ranges of the parameters sampled in the MCMC framework are given in Table 1. In total, we consider 10 parameters in the MCMC algorithm.

Given that MCMC explicitly samples from the parameter PDF and then updates this PDF, the danger of overfitting these parameters to the observations is minimal. The radar variables exhibit function dependency on height and are related to each other, owing to the ongoing microphysical processes. These relations limit the potential degrees of freedom represented by the observations, reducing the change of overfitting parameters to the observations. Empirical evidence suggests that overfitting does not occur, where the resulting parameter PDFs in the following section show nonzero probability densities over plausible ranges of the parameter values.

4. Results

a. Radar-profile simulations

As a first step in evaluating the parameter estimation framework, we examine its ability to successfully reproduce the observed radar fingerprints of vapor depositional growth associated with this case. The simulated vertical profiles of Z, Z_{DR}, and MDV, derived from a sample of parameters drawn from the MCMC posterior distribution, are shown in Fig. 7, along with the corresponding observed profiles. Overall, there is good agreement between the simulated and observed fields in terms of magnitudes and qualitative trends, as the modeled profiles generally lie within the error bounds of the observations. The simulated Z_{DR} profiles have values that are between 5 and 7 dB, with most profiles having Z_{DR} values below the mean observed Z_{DR}. The MDV profiles have values generally greater than the observed mean MDV below 1300 m AGL and have values generally less than the observed mean MDV above 1400 m AGL. In addition, there is a relatively large amount of variability in the Z and MDV gradients near the top of the profiles at heights > 1500 m AGL. This altitude may correspond to the rapid initial growth of planar crystals, and therefore could be highly sensitive to the prescribed Γ and updraft parameters that perturb the environmental s_i.

Owing to the sensitivity of the simulated MDV to the particle fall speed, the method we use for calculating the particle fall speed (Mitchell 1996) may introduce additional structural uncertainty into our results. In our simulations, the particle fall speed is determined by simulated maximum dimension, aspect ratio, and area ratio (i.e., effective density divided by particle volume), where these particle properties are inputs to the Mitchell (1996) fall speed parameterization. Given the uncertainties in natural branched planar crystal fall speeds (e.g., Kajikawa 1972), it is likely that there are additional uncertainties in the fall speed beyond those determined by the sampled ice growth parameters. Additional perturbations on the simulated velocity of 0.1–0.2 $\mathrm{m\,s}^{-1}$ [on the order of the variability from Kajikawa (1972)] would increase the range of simulated MDV profiles, with the more negative profiles likely to match the observed profiles better between 1000 and 1200 m (Fig. 7).

Another important test of these results is to evaluate the physical validity of the MCMC-derived flow fields (determined by the PDF of the updraft parameters). For example, Shupe et al. (2008) examine vertical velocities associated with thin, single-layer Arctic clouds in the fall transition season, and found the vertical velocity mean amplitude was 0.66 m s^{-1}, with a standard deviation of 0.19 m s^{-1} for their study period. By comparison, the vertical motion profiles within the updraft region of our simulations have smaller values; a sample of 100 kinematic parameters drawn from the posterior distribution of the MCMC framework shows maximum vertical velocities <0.2 m s^{-1}, with values mostly between 0.02 and 0.08 m s^{-1} (Fig. 9). There is limited availability of KAZR data above the cloud base (~1.6 km), perhaps owing to limited sensitivity or the thin nature of the cloud. As such, reliable vertical motion estimates from the instrument are unavailable. However, the MDV data show almost exclusively inbound hydrometeor vertical motion [toward the radar; in contrast to larger inbound and outbound velocity magnitudes shown by Shupe et al. (2008)], with the least negative MDV values (~ −0.2 to −0.1 m s^{-1}) near cloud top. Given that ice particles in this region of the cloud have the smallest sizes and terminal fall speeds, the simulated vertical motion profiles in Fig. 9 are likely of similar magnitude as those occurring naturally during this case. Right at and below cloud base, variations in KAZR spectra (not shown) are several tenths of a m s^{-1}, suggesting that stronger vertical motions are not present there.

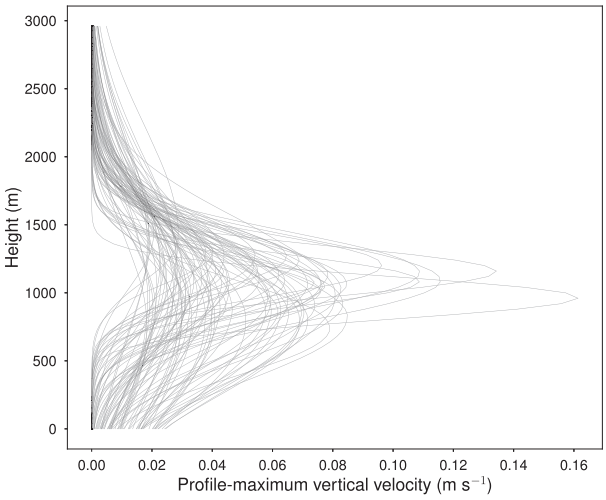

FIG. 9. Ensemble of simulated vertical velocity profiles using 100 samples from the posterior distribution determined from the MCMC framework.

b. *Relations between MCMC-sampled model parameters*

To analyze the relations between the uncertain parameters perturbed herein, we examine the posterior joint PDFs of the parameters (shown in Fig. 10). To simplify the visualization of this multidimensional parameter space, each panel shows the joint two-dimensional marginal PDF between two of the uncertain parameters. The diagonal of this "corner plot" represents the one-dimensional marginal distributions. Darker shading represents a higher density of points sampled in that region of the space, and thus greater probability that the true parameter value is found there.

Several of the marginal PDFs show clear maxima in the most probable parameter values for this case. In particular, C_{IGR}, f_b, N_{ice}, C_{w_s}, C_{d_s}, and C_{Z_0} show relatively narrow ranges in values with maximum probability densities, suggesting the radar observations provide meaningful constraints on these uncertain parameters (Fig. 10). Thus, we can derive some insight into the validity of theoretical assumptions about branched planar crystal growth from these most probable parameter values.

For example, the peak in C_{IGR} is around 2.0, a higher $\Gamma(T)$ near −15°C than the value suggested by Chen and Lamb (1994), but one that is closer to the higher values suggested by Sei and Gonda (1989). Since the deposition coefficients vary in time for faceted crystals, the ratio of the deposition coefficients can cover a very large range (see Fig. 12a in Harrington et al. 2019), which includes the values of Sei and Gonda (1989) and Chen and Lamb (1994).

Harrington et al. (2019) show that it is better to compare $\Gamma(T)\phi$ predicted by the Chen and Lamb (1994) model to laboratory measured ratios of the deposition coefficient (α_c/α_a) because measured faceted crystals tend to follow the growth law $dc/da = \alpha_c/\alpha_a$, whereas the Chen and Lamb (1994) model (upon which our model is based) follows the growth law $dc/da = \Gamma(T)\phi$. Thus, it is more consistent to compare measured α_c/α_a to $\Gamma(T)\phi$ calculated from the Chen and Lamb (1994) model. This comparison is shown in Fig. 11 for deposition coefficient ratios extracted from wind tunnel measurements of dendritic growth at constant temperature, and at liquid saturation using best fits to theoretical calculations (green shaded region). The crystals were grown for about 15 min, which is a similar time scale to the growth of the crystals modeled here. The purple points show the values of $\Gamma(T)\phi$ from the parameter PDF. Ice particles grown in the kinematic model simulations do so over a range of temperatures, and so the values of $\Gamma(T)\phi$ are not strictly associated with a single temperature. To show the range of the parameter PDF values and how it compares to the laboratory-extracted values, $\Gamma(T)\phi$ is randomly scattered with cloud temperature. It is immediately clear from the figure that the parameter PDF estimates of $\Gamma(T)\phi$ fall almost completely within the range of values extracted from laboratory measurements, between 0.003 and 0.05. The parameter PDF estimates are relatively flat across temperature, owing to the temperatures ranging from about −12° to −18°C. The laboratory values (tabulated at individual temperatures) show a strong minimum at −15°C. Nevertheless, these results increase the degree of confidence in the parameter PDF values estimated via MCMC.

Similar to the comparison of the deposition coefficient ratio, the peak in the f_b (smaller values indicate thinner and/or fewer subbranches) PDF is concentrated between 30% and 50%, suggesting a moderate density of crystal subbranches (Fig. 10). In contrast, the marginal PDFs for the f_t, f_i, a_c, and C_a parameters (which describe the fractional tip width, the inscribed hexagon length fraction, and the characteristic size scaling factor) appear to have nearly equally likely values across their full ranges, suggesting limited constraining

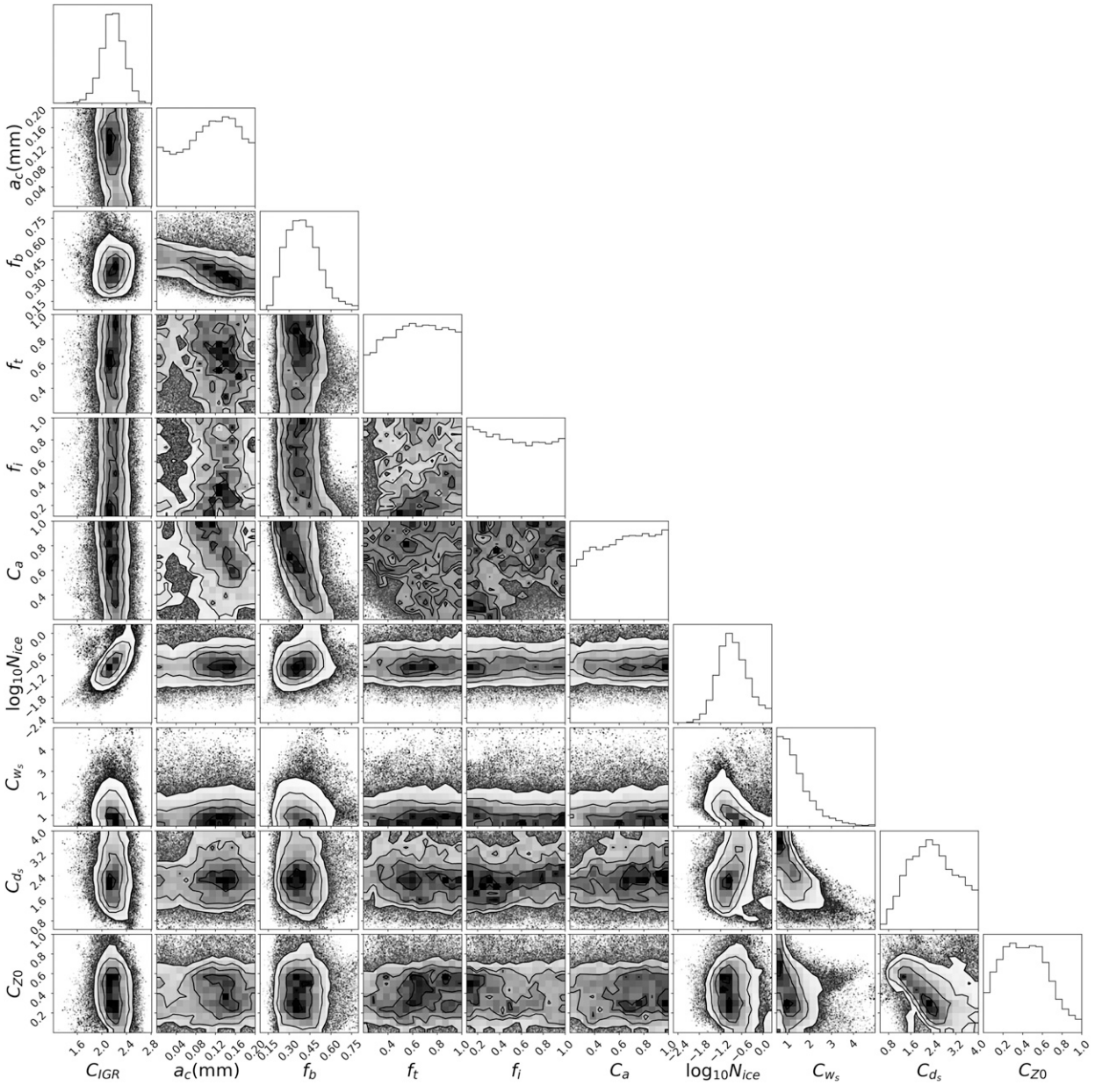

FIG. 10. Parameter posterior PDF for the default simulation, constrained by X-SAPR Z and Z_{DR}, and KAZR Z and MDV. The shading represents relative frequencies within each joint PDF, normalized by the maximum relative frequency within the joint PDF. Four evenly spaced contours of the normalized relative frequency are plotted in each joint PDF as a visualization aid.

information about these parameters from the radar observations. The C_{d_s} values are more strongly constrained and centered around 1.4, suggesting that our initial 2D circulations were about 40% too narrow. Additionally, the most probable values of N_{ice} are around $0.04\,L^{-1}$. However, N_{ice} shows a strong functional relation with mean maximum dimension, where higher values of N_{ice} correspond to smaller maximum dimension values (Fig. 12).

Despite the relatively uniform marginal PDFs for the other ice crystal structure parameters, samples of ρ_{eff} curves derived from the MCMC posterior PDF show some consistent behavior (Fig. 13). Generally speaking, these curves show steep initial declines in ρ_{eff} for $a > a_c$—though not as steep as those with assumed constant ρ_{dep}—that become more gradual as a increases, resulting in minimum ρ_{eff} between 200 and $500\,kg\,m^{-3}$, with the median ρ_{eff} at $a = 3$ mm of $330\,kg\,m^{-3}$. This value is only modestly above that suggested by J17 and Chen and Lamb (1994) near −15°C, suggesting some potential correspondence with laboratory measurements of ρ_{eff} for larger particles. To visualize the range of crystal structures corresponding to the MCMC-sampled parameters from this event, crystals generated based on 100 samples from the

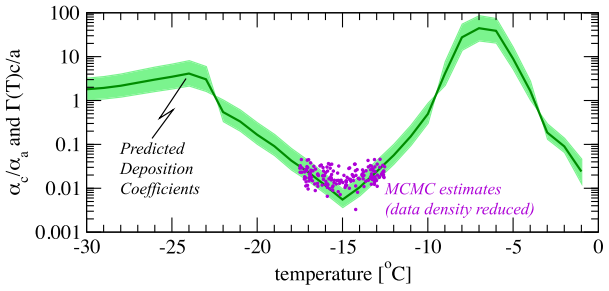

FIG. 11. Ratio of deposition coefficients for the c and a axes of crystals extracted from wind tunnel measurements of ice crystal growth at liquid saturation and constant temperature (green solid curve) and the uncertainty range (green shade) from Harrington et al. (2019). Purple points are $\Gamma \times \phi$ from the MCMC parameter PDF. For clarity, only a subset of the points from the PDF are shown and these are scattered randomly over the temperature range of the observed cloud layer (−12° to −18°C).

maximum a posteriori PDF are shown in Fig. 14. Though obviously artificial (e.g., we plot them all with four subbranches per main branch and at $a = 3$ mm), the simulated shapes compare favorably to the crystals shown in Oue et al. (2016).

Joint PDFs of the perturbed parameters (Fig. 10) reveal several clear relationships. Most notably, there is a positive correlation between C_{IGR} and N_{ice}. For smaller C_{IGR}, the ice particles grow more rapidly (as evident in the negative correlation between C_{IGR} and maximum dimension in Fig. 12) and therefore a smaller number concentration is needed to produce the same Z that falls within the observational uncertainty. N_{ice} also has a negative correlation to the updraft magnitude factor C_{w_s}, owing to the increased s_i associated with larger vertical motions; these more favorable growth conditions produce larger particles that in turn have reduced N_{ice} to agree with the Z observations (Fig. 10). The updraft depth factor C_{d_s} also shows negative correlations with C_{w_s}, as increases in the magnitude of the flow field are balanced by decreases in the circulation depth to preserve similar s_i above 1 km. The vertical velocity profiles in Fig. 9 also show the MCMC-derived inverse correlation between C_{w_s} and C_{d_s}, where the largest vertical motions occur within the sharpest peaks in vertical velocity with respect to height. Similarly, the updraft centroid height factor C_{Z_0} is negatively correlated with C_{w_s}, where a higher updraft centroid generally increases the supersaturation in the upper region of the cloud (>1 km AGL); lower values of C_{w_s} may then offset these increases in supersaturation. Similar reasoning also explains the negative correlation between C_{d_s} and C_{Z_0} (Fig. 10).

In contrast, many of the parameters show minimal dependence on the ice structure parameters f_t, f_i, a_c, and C_a (tip width fraction, inscribing hexagon fraction, ice core size, and characteristic size scaling factor, respectively), corresponding to their more uniform marginal PDFs. One modest exception is a slight negative correlation between f_i and f_b for values of $f_i < 0.3$. In this region, lower values of f_i require higher values of f_b to maintain the same ρ_{eff}. As f_i increases, f_b has a larger influence on ρ_{eff} (especially because the mean particle size is $\leq a_i$; Fig. 8) and changes in f_i result in minimal changes in effective density. a_c also shows a negative correlation to f_b, as lower a_c values require higher f_b values to maintain a similar ρ_{eff} (and thus Z_{DR} within the range of observational variability). For similar reasons, f_b also shows a negative correlation to C_a (Fig. 10).

c. *Relations between the MCMC parameters and the radar variables*

Figure 15 shows joint PDFs between the uncertain model parameters and the profile-mean simulated radar variables between 1.0 and 1.5 km. These represent the sensitivity of radar variables to *joint* perturbation of parameters according to their posterior probability (i.e., they do not represent one-at-a-time sensitivities). We note cases where correlations are evident, but do not comment on cases where no correlation is obvious because relationships between parameters and radar variables may be obscured by compensating multivariate parameter perturbations. Indeed, any parameters that are well constrained by the observations must have some controlling influence over their forward-simulated values.

The first column of Fig. 15 shows the relationships between mean Z, mean Z_{DR}, and mean MDV with C_{IGR}. C_{IGR} is negatively correlated with both mean Z_{DR} and mean MDV, the former showing a stronger relation compared to the latter.

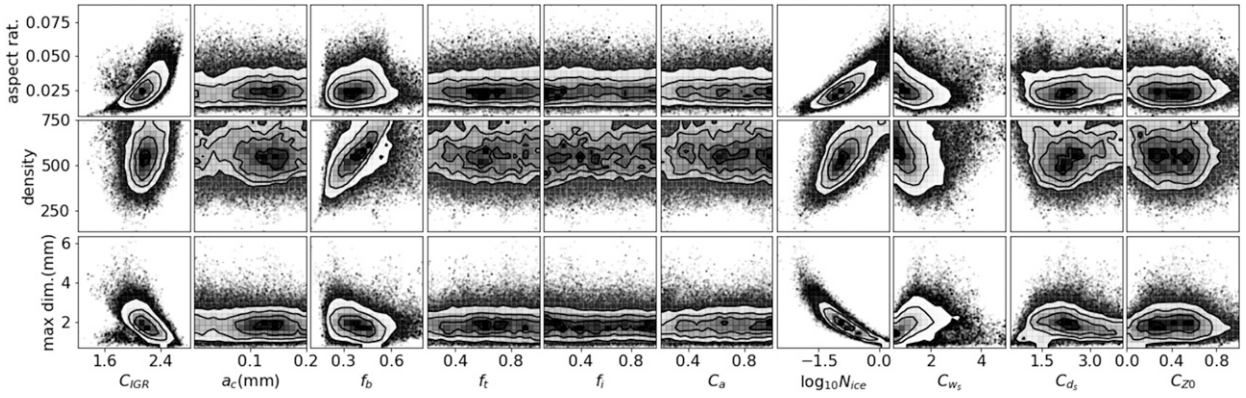

FIG. 12. Joint posterior PDF of parameters and microphysical quantities: (top) aspect ratio, (middle) density, and (bottom) number-weighted maximum diameter. The shading and contours are as described for Fig. 10.

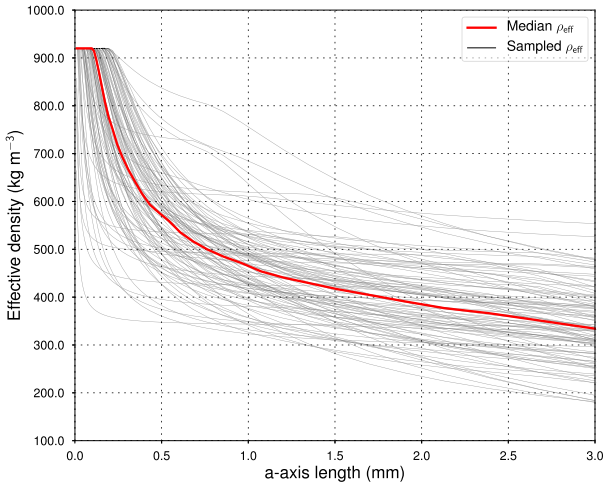

FIG. 13. Effective density curves for each of the 100 sampled parameters from the MCMC-derived posterior distribution (black lines) and the median effective density curve (red line).

Greater values of C_{IGR} represent larger Γ at a given T and, thus, crystals with less accentuated aspect ratios (higher ϕ) with smaller Z_{DR} and larger terminal fall speeds are produced. However, these particles may grow slower than those with lower C_{IGR}, thereby somewhat offsetting the increases in terminal fall speed with time.

There is a positive correlation between the subbranch coverage fraction f_b and mean Z_{DR} (Fig. 15): larger fractional coverage by subbranches means the simulated crystals have greater ρ_{eff} and thus greater Z_{DR} for a given shape (e.g., SK19). Likewise, increased f_b contributes to greater fall speeds and thus more negative mean MDV, though this relation is somewhat muted given the influence of the kinematic flow parameters on MDV and variability in ϕ from perturbations on C_{IGR}.

The profile-mean radar variables also exhibit some dependence on N_{ice} (Fig. 15). The mean Z is larger for larger N_{ice}; larger N_{ice} is also associated with smaller mean Z_{DR} and more negative mean MDV (i.e., faster-falling particles). The increased competition of the ice crystals for the same supply of vapor leads to smaller and generally denser particles (Fig. 12). Because of the strong positive correlation between N_{ice} and C_{IGR} (Fig. 10), these particles also have higher ϕ and therefore larger fall speeds (as observed in Fukuta and Takahashi 1999) and smaller Z_{DR}.

Previous work has shown that the vertical gradients of radar variables also provide fingerprints of ongoing microphysical processes (e.g., Yuter and Houze 1995; Fabry and Zawadzki 1995; Cifelli et al. 2002; Kumjian and Ryzhkov 2010, 2012; Schneebeli et al. 2013; Ryzhkov et al. 2013; Kumjian and Prat 2014; Schrom and Kumjian 2016; Kumjian and Lombardo 2017; Dias Neto et al. 2019). Thus, we expect that the gradients of the simulated radar variables should be related to some of the particle-property model parameters. Indeed, Fig. 16 reveals such relationships. For Fig. 16, positive gradients indicate larger magnitudes toward the ground. Both Z and MDV gradients have positive correlations with C_{IGR}, C_{w_s}, and N_{ice} (Fig. 16). The latter two favor increased total mass growth, and thus increased gradients in these variables. However, larger C_{IGR} values are associated with slower mass growth and more compact, higher-ϕ particles; these faster-falling particles would be positively correlated with gradients in MDV (e.g., Schrom and Kumjian 2016), but not necessarily positively correlated with gradients in Z. We suspect that the correlation with Z is simply due to C_{IGR} being highly correlated with N_{ice}.

The Z_{DR} gradients are mostly negative (i.e., Z_{DR} decreases toward the ground), with the most common values around $-1\,\mathrm{dB\,km^{-1}}$ (Fig. 16). The joint PDFs show slight negative correlations with C_{IGR} and slight positive correlations with subbranch coverage factor f_b. Larger C_{IGR} values suggest higher-ϕ particles and thus the decreasing ρ_{eff} accompanying growth as the particles fall causes slightly larger decreases in Z_{DR} compared to particles with smaller ϕ, where Z_{DR} decreases less toward the ground. Larger f_b values are associated with smaller decreases in ρ_{eff} with growth, and therefore Z_{DR} decreases slightly or is nearly constant with growth, producing the negative correlation between f_b and the gradient in Z_{DR}.

Finally, we examine the impact different sets of observations used to guide the MCMC parameter estimation framework have on the results. Figure 17 shows the marginal PDFs for several of the uncertain parameters using all of the observations, using just the KAZR observations (i.e., Z and MDV), and using just the X-SAPR observations (i.e., Z and Z_{DR}). Overall, simulations using all of the observations showed the narrowest marginal PDFs, and therefore produce the highest confidence parameter estimates. For example, the mode of the C_{IGR} PDF has maximum density values ~50% larger for the full-observation results compared to the KAZR-only results; also, low values of f_b (i.e., very sparse crystal structures) are found to be less probable upon inclusion of the X-SAPR observations. In some cases, the modes of the PDFs between the three observational experiments differ substantially; for N_{ice}, the X-SAPR-only maximum probability value is around an order of magnitude less than the estimate from the KAZR-only and full-observation experiments. Some of these differences may be explained by differences in the averaging regions of KAZR and X-SAPR. Generally, the KAZR-only experiment provides parameter PDFs that are much closer to the full-observation experiment than the X-SAPR-only experiment, suggesting that for the parameters perturbed in this study, MDV and Z contain most of the useful constraining information. One reason Z_{DR} may be less useful for this case is that the observed Z_{DR} profiles for this case are relatively constant with height. Therefore, the sample space of microphysical and kinematic parameters that produce the near constant value of Z_{DR} is much larger compared to the sample space that can produce the large gradients observed in the Z and MDV profiles.

5. Summary and conclusions

Overall, the MCMC-sampling framework successfully generates PDFs of the perturbed microphysical and kinematic parameters, while also producing simulated radar profiles consistent with the observations. The derived parameter PDFs show that the simplified model framework captures realistic modes of microphysical variability within the Arctic cloud. For example, these parameter PDFs produce simulations where

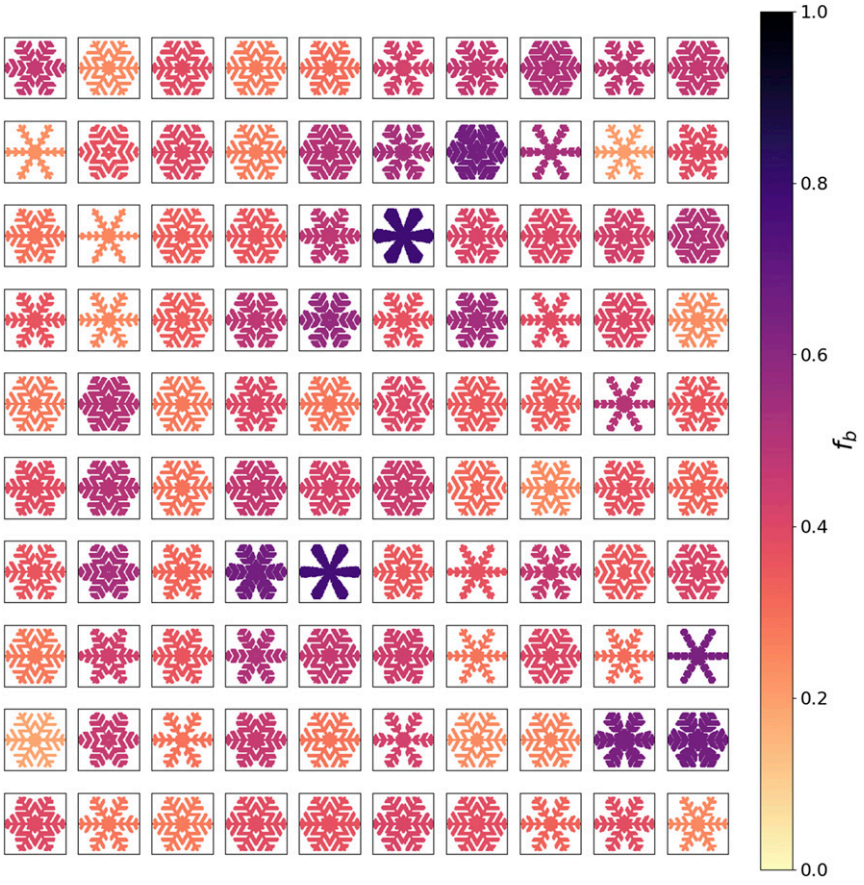

FIG. 14. Crystals generated based on 100 parameters drawn from the MCMC-derived parameter PDF. The colors indicate the f_b value (the fractional area coverage of the sub branches) for each sample.

the target number concentration is correlated with both aspect ratio and density. These correlations result from an increasing number of ice particles competing for the ambient vapor supply, decreasing the mean particle size; the inverse correlations between size and both aspect ratio and density then produce the observed behavior. The relative simplicity of the relations between parameters suggests that using a more efficient method to sample the parameter PDFs may be justified for this framework.

These ambiguities in the particle properties also suggest that additional radar variables (such as LDR, ρ_{hv}, and K_{dp})

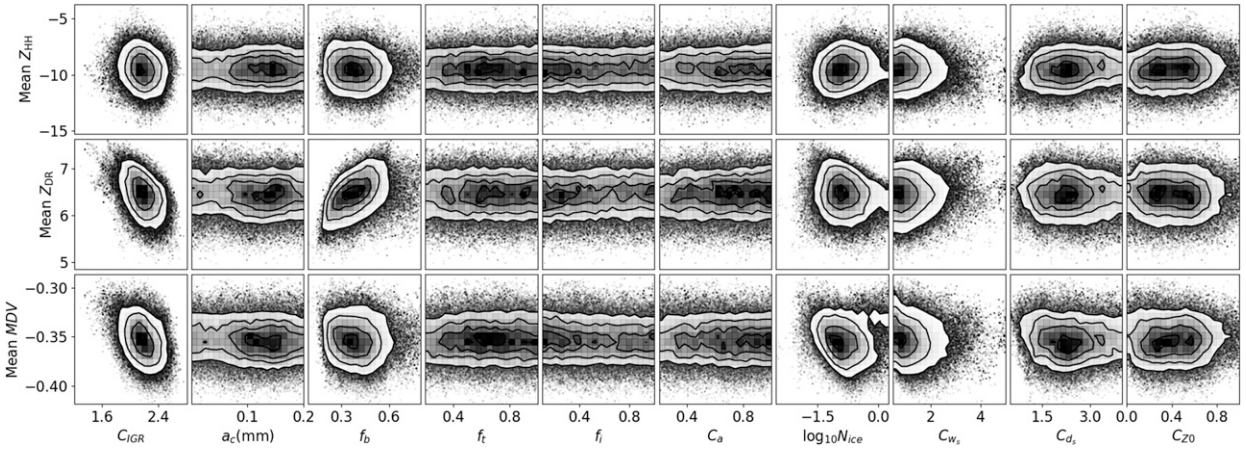

FIG. 15. Joint posterior PDF of parameters and profile-mean radar quantities. The shading and contours are as described for Fig. 10.

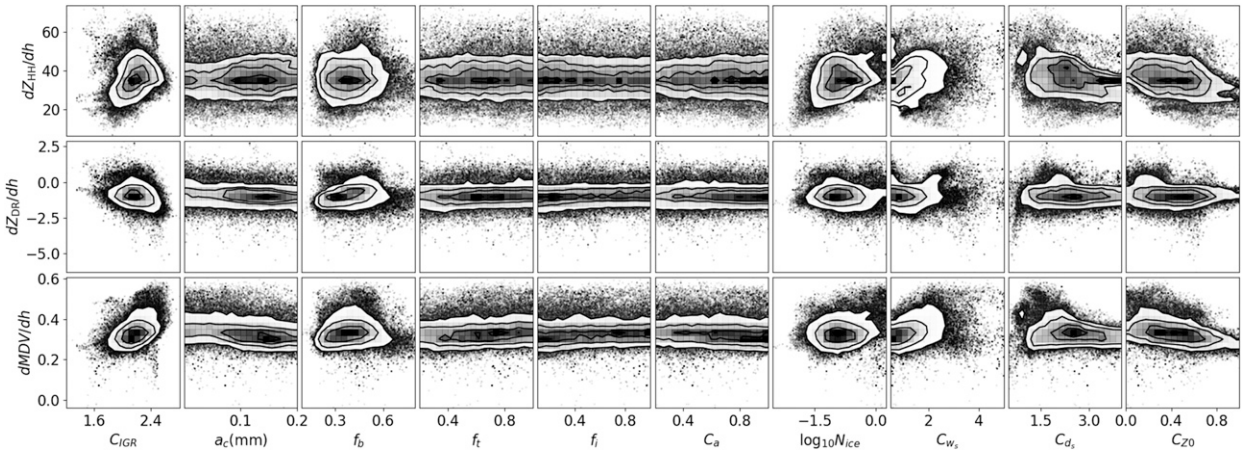

FIG. 16. As in Fig. 15, but for profile gradients of radar variables.

could help to further constrain the microphysical parameters of vapor growth. In particular, additional independent constraints on the number concentration are needed in order to more effectively constrain the ice particle structure parameters. Owing to its strong dependence on number concentration, $K_{\rm dp}$ may be useful in this regard; changes in the shape parameter of the PSD can have a dramatic impact on the number of small particles and therefore $K_{\rm dp}$ may help constrain this parameter as well.

Of the ice crystal structure parameters we consider herein, only the subbranch coverage fraction f_b (and to a minor extent, the ice core size a_c) has a significant impact on the radar variables, and similarly has significant covariances with the microphysical parameters. Thus, a more simplified deposition density (and corresponding effective density) function may be suitable for microphysical modeling or remote sensing retrieval purposes. In particular, the median effective density curve shown in Fig. 13 illustrates a promising candidate for such a function. Only a_c, $a_{\rm max}$, and a limiting effective density $\rho_{a_{\rm max}} = \rho_{\rm eff}(a_{\rm max})$ could be used to define this function, where the curvature of effective density corresponds to the median effective density from the posterior-PDF-sampled parameters. However, this $\rho_{\rm eff}$ curve decreases more gradually than those of the fixed-$\rho_{\rm dep}$ model and thus produces more realistic $Z_{\rm DR}$ behavior and corresponds to more realistic physical structures.

The small variability in $Z_{\rm DR}$ with growth, where both effective density and aspect ratio decrease, for the assumed particle shapes causes a natural limitation in the information content of $Z_{\rm DR}$ for cases of branched planar crystal growth. For example, the largest changes in $Z_{\rm DR}$ occur during the initial growth as a plate; the decrease in aspect ratio with constant density greatly increases $Z_{\rm DR}$. As branched growth occurs, the decrease in aspect ratio is offset somewhat by the decrease in effective density, and $Z_{\rm DR}$ is confined within a narrow range of

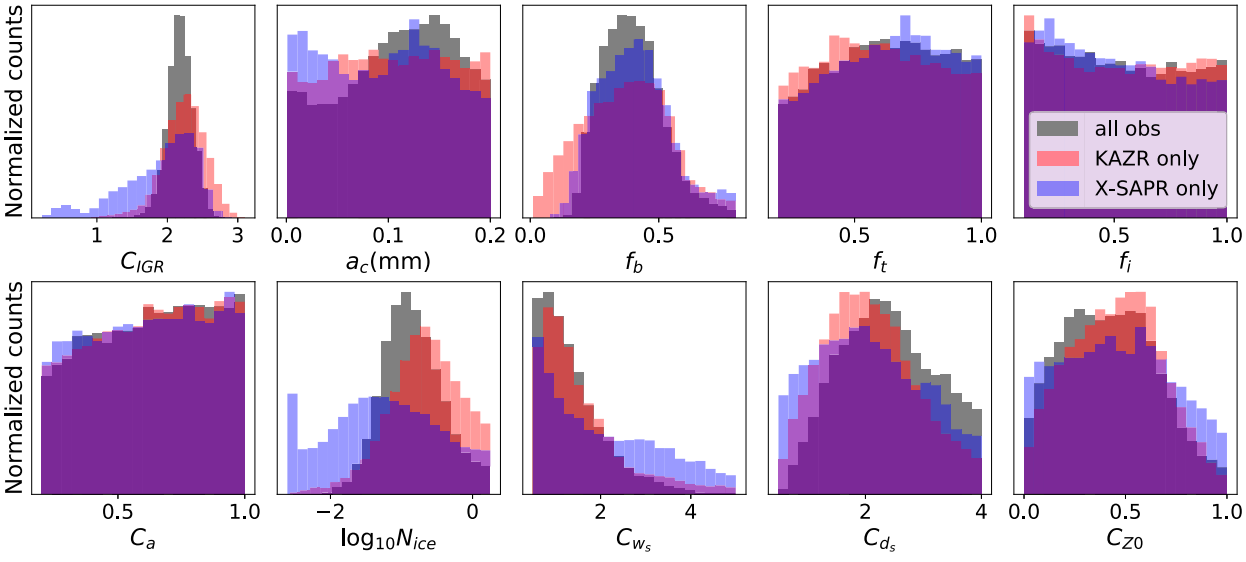

FIG. 17. Marginal PDFs of parameters for experiments using both KAZR and X-SAPR as constraints (gray), KAZR only as a constraint (red), and X-SAPR only as a constraint (blue).

values. Therefore, the ability of Z_{DR} to constrain the effective density evolution of these particles is somewhat limited. The MCMC parameter estimation framework does highlight a specific range of subbranch coverage fraction (f_b) values; however, the relatively large standard deviation associated with the estimate for this parameter illustrates the limited ability to constrain density evolution. In contrast, the Z and MDV profiles are stronger constraints on the density evolution of branched planar crystals. This may, in part, be related to the greater sensitivity of the KAZR compared with the X-SAPR, which allows it to observe at greater elevations in the cloud. We expect that Z_{DR} offers more information for other microphysical processes, including aggregation (e.g., Schrom and Kumjian 2016).

Despite the relatively idealized nature of this study, the maximum likelihood parameter values derived from MCMC fall within the general range of values from laboratory measurements and theoretical calculations derived from such measurements. These favorable comparisons provide further evidence that our Bayesian framework can provide useful constraints on ice microphysical processes, though inherently subject to averaging effects over a range of environmental conditions. These averaging effects arise from the fact that growth occurs along the trajectories of the particles through different regions of the domain. Additionally, the simplified, stationary flow field also provides a sort of averaging effect on the derived parameters, given that the flow in natural clouds exhibits, time-varying, finescale features such as generating cells and turbulence. Even if our model could represent these processes, there will always be discrepancies between simulations and observations, given the potentially large variability in ice particle properties over short time scales and small spatial scales. Therefore, any comparison between simulated and observed radar variables requires considering enough observations (and model-simulated observations) such that comparisons between the statistical distributions of the natural and simulated processes can be considered meaningfully different from each other to guide MCMC.

Given the need to better understand ice particle growth over a large range of thermodynamic environments, our results suggest that vapor deposition at different temperatures and/or ongoing riming and aggregation can also be better constrained using a similar framework. Incorporating vapor growth outside of the planar crystal regime, as well as for more irregular ice particles, would require considering different structure parameters (such as degree of hollowing for columns) during growth. Determining a method to realistically evolve the ice structure may prove more challenging for irregular pristine ice crystals.

The increased complexity of aggregation and riming would also require increasing the set of microphysical model and ice particle shape parameters used in the parameter estimation procedure. For riming, parameters governing the collection efficiency of supercooled liquid, as well as the shape evolution of the particles would need to be included. Similar parameters could be included to apply this framework to aggregation. Additionally, the radar forward model would need to be extended to accurately simulate the scattering properties of aggregates and rimed particles. Several scattering databases that include these particles already exist (e.g., Lu et al. 2016; Kuo et al. 2016), and could be exploited to extend the forward model. Given the increased complexity of these processes, additional radar observables such as ρ_{hv}, K_{dp}, LDR, and dual-frequency measurements would be needed to effectively constrain the more extensive parameter set. Increased in situ observations may also help constrain detailed particle properties.

TABLE A1. Description of quantities used in the size-dependent deposition density formulation.

Quantity	Description
a_c	Core a-axis side length
a_{max}	Crystal maximum a-axis length
a_i	Crystal inscribed a-axis length
w_{mb}	Main branch width
w_t	Bounding star tip width
f_b	Subbranch fractional area coverage
f_t	Tip width fraction
f_i	Inscribed hexagon fractional distance
f_{mb}	Main branch fractional width
ρ_i	Density of solid ice
ρ_{dep}	Deposition density

Acknowledgments. We thank the three anonymous reviewers of this manuscript for their insightful and beneficial comments. The authors were funded through DOE Grant DE-SC0018933, excluding RS, who was supported by an appointment to the NASA Postdoctoral Program at the NASA Goddard Space Flight Center, administered by Universities Space Research Association under contract with NASA. Components of this manuscript are part of the first author's Ph.D. dissertation. NCAR is supported by the National Science Foundation.

Data availability statement. The radar observations used herein are part of a special intense observing period at the North Slope Alaska ARM site during May 2013, and unfortunately are not publicly available. As such, we provide these data upon request.

APPENDIX

Size-Dependent Deposition Density Formulation

The main assumption used to adapt the SK19 crystal generation method for our size-dependent deposition density model is that the discretely spaced subbranches from the synthetic crystal shapes can be adequately represented by a continuous areal subbranch coverage fraction f_b. A listing and corresponding description for each of the quantities we use in this deposition density formulation are given in Table A1. Given the assumed sixfold symmetry of ice crystals, we can simply consider ρ_{dep} over one of the six equilateral triangular sections composing the structure (as depicted in Fig. A1). SK19 define the crystal structure by considering three regions in each of these six identical, triangular sections (Fig. A1) defined by sizes a_c, a_i, and a_{max} (depicted in Fig. A2):

1) Region 1 is within a solid-ice core ($a \leq a_c$).

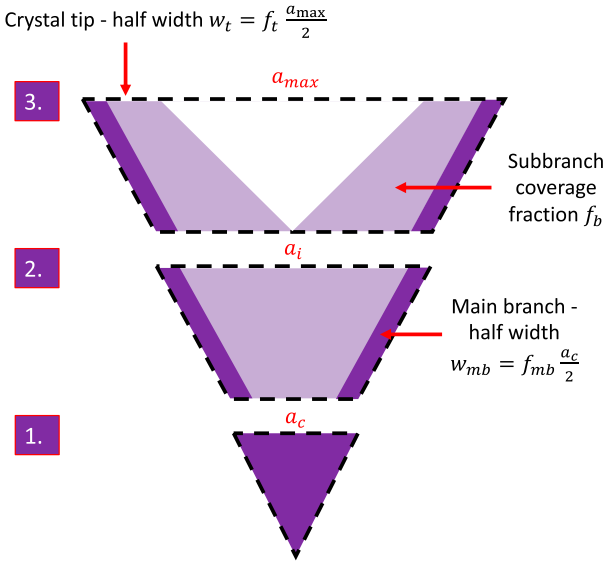

FIG. A1. Diagram of the three regions determining the analytical, size-dependent deposition density described herein. Given the sixfold symmetry of the branched planar crystals, the plot shows one of the six identical triangular sections of an idealized branched planar crystal (cf. to the generated shape in Fig. A2). The dark purple regions indicate solid ice regions with density ρ_i and the lighter purple regions indicate homogeneous regions of density $f_b\rho_i$.

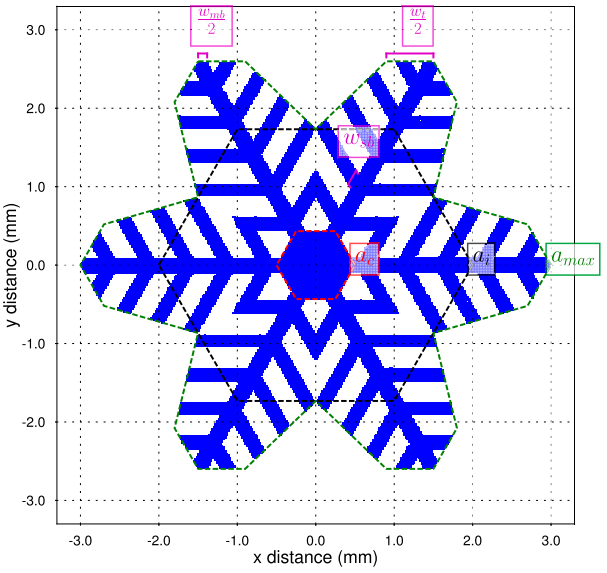

FIG. A2. Plot of crystal regions. Adapted from SK19.

2) Region 2 is between the edge of the solid-ice core and an inscribed hexagon ($a_c < a \le a_i$). In this region, the main branches of half-width w_{mb}[A1] grow off of the core and subbranches between the main branches provide area coverage fraction f_b. The inscribed hexagon length a_i must be between a_c and a_{max}, and thus we define the inscribed hexagon length fraction $f_i = (a_i - a_c)/(a_{max} - a_c)$.
3) Region 3 is between the edge of the inscribed hexagon and the maximum extent of the crystal ($a_i < a \le a_{max}$). The main branches in this region are consistent with region 2, and this region also has the same fractional subbranch coverage as region 2. However, the subbranch coverage area is limited by a horizontally centered triangle with base at a_{max} and tip at (a_i. The base of this triangular region has length $a_{max}-2w_t$ (where w_t is defined as the crystal tip width) and has height $a_{max}-a_i$. We also define a fractional tip width $f_t = 2w_t/a_{max}$, constrained to range in value from $f_{mb} \times (a_c/a_{max})$ to 1 so that $w_{mb} \le w_t \le a_{max}/2$.

Because a_{max} is unknown, we assume a value of 3 mm, representing the higher end of branched planar crystal sizes. However, this value can be scaled along with a to represent the same structure at larger or smaller sizes.

From the assumption of planar crystal growth, the deposition density is

$$\rho_{dep}(a) = \rho_i f_{dep}(a). \tag{A1}$$

In the limit as the change in a-axis length goes to zero (i.e., infinitesimal growth), f_{dep} becomes the ratio of the linear coverage fraction alongside length a and a, giving

$$f_{dep}(a) = \begin{cases} 1, & \text{if} \quad a \le a_c \\ f_b + \dfrac{a_c}{a}(1-f_b)f_{mb}, & \text{if} \quad a_c < a \le a_i \\ \dfrac{f_b}{a_{max}-a_i}\left[f_t a_{max} - a_i + (1-f_t)\dfrac{a_i a_{max}}{a}\right] + \dfrac{a_c}{a}(1-f_b)f_{mb}, & \text{if} \quad a_i < a \le a_{max}. \end{cases} \tag{A2}$$

[A1] We express w_{mb} in terms of the main branch fraction f_{mb} with $W_{mb} = f_{mb} \times (a_c/2)$.

REFERENCES

Andrić, J., M. R. Kumjian, D. S. Zrnić, J. M. Straka, and V. M. Melnikov, 2013: Polarimetric signatures above the melting layer in winter storms: An observational and modeling study. *J. Appl. Meteor. Climatol.*, **52**, 682–700, https://doi.org/10.1175/JAMC-D-12-028.1.

Avramov, A., and J. Y. Harrington, 2010: The influence of parameterized ice habit on simulated mixed-phase Arctic clouds. *J. Geophys. Res.*, **115**, D03205, https://doi.org/10.1029/2009JD012108.

Bailey, M., and J. Hallett, 2009: A comprehensive habit diagram for atmospheric ice crystals: Confirmation from laboratory, AIRS II, and other field studies. *J. Atmos. Sci.*, **66**, 2888–2899, https://doi.org/10.1175/2009JAS2883.1.

Baker, B. A., and R. P. Lawson, 2006: In situ observations of the microphysical properties of wave, cirrus, and anvil clouds. Part I: Wave clouds. *J. Atmos. Sci.*, **63**, 3160–3185, https://doi.org/10.1175/JAS3802.1.

Brown, P. R. A., and P. N. Francis, 1995: Improved measurements of the ice water content in cirrus using a total-water probe. *J. Atmos. Oceanic Technol.*, **12**, 410–414, https://doi.org/10.1175/1520-0426(1995)012<0410:IMOTIW>2.0.CO;2.

Chen, J.-P., and D. Lamb, 1994: The theoretical basis for the parameterization of ice crystal habits: Growth by vapor deposition. *J. Atmos. Sci.*, **51**, 1206–1222, https://doi.org/10.1175/1520-0469(1994)051<1206:TTBFTP>2.0.CO;2.

——, and ——, 1999: Simulation of cloud microphysical and chemical processes using a multicomponent framework. Part II: Microphysical evolution of a winter orographic cloud. *J. Atmos. Sci.*, **56**, 2293–2312, https://doi.org/10.1175/1520-0469(1999)056<2293:SOCMAC>2.0.CO;2.

——, and T.-C. Tsai, 2016: Triple-moment modal parameterization for the adaptive growth habit of pristine ice crystals. *J. Atmos. Sci.*, **73**, 2105–2122, https://doi.org/10.1175/JAS-D-15-0220.1.

Cifelli, R., W. A. Petersen, L. D. Carey, and S. A. Rutledge, 2002: Radar observations of the kinematic, microphysical, and precipitation characteristics of two radar observations of the kinematic, microphysical, and precipitation characteristics of two MCSs in TRMM LBAMCSs in TRMM LBA. *J. Geophys. Res.*, **107**, 8077, https://doi.org/10.1029/2000JD000264.

Cotton, W. R., 1972: Numerical simulation of precipitation development in supercooled cumuli: Part II. *Mon. Wea. Rev.*, **100**, 764–784, https://doi.org/10.1175/1520-0493(1972)100<0764:NSOPDI>2.3.CO;2.

Dias Neto, J., and Coauthors, 2019: The Triple-Frequency And Polarimetric Radar Experiment for improving process observations of winter precipitation. *Earth Syst. Sci. Data*, **11**, 845–863, https://doi.org/10.5194/essd-11-845-2019.

Fabry, F., and I. Zawadzki, 1995: Long-term radar observations of the melting layer of precipitation and their interpretation. *J. Atmos. Sci.*, **52**, 838–851, https://doi.org/10.1175/1520-0469(1995)052<0838:LTROOT>2.0.CO;2.

Fridlind, A. M., A. S. Ackerman, G. McFarquhar, G. Zhang, M. R. Poellot, P. J. DeMott, A. J. Prenni, and A. J. Heymsfield, 2007: Ice properties of single-layer stratocumulus during the Mixed-Phase Arctic Clouds Experiment (M-PACE): Part II: Model results. *J. Geophys. Res.*, **112**, D24202, https://doi.org/10.1029/2007JD008646.

Fukuta, N., and T. Takahashi, 1999: The growth of atmospheric ice crystals: A summary of findings in vertical supercooled cloud tunnel studies. *J. Atmos. Sci.*, **56**, 1963–1979, https://doi.org/10.1175/1520-0469(1999)056<1963:TGOAIC>2.0.CO;2.

Gaustad, K. L., D. D. Turner, and S. A. McFarlane, 2011: MWRRET value-added product: The retrieval of liquid water path and precipitable water vapor from Microwave Radiometer (MWR) data sets. DOE Tech. Rep. DOE/SC-ARM/TR-081.2, 19 pp.

Giangrande, S. E., T. Toto, A. Bansemer, M. R. Kumjian, S. Mishra, and A. V. Ryzhkov, 2016: Insights into riming, aggregation processes as revealed by aircraft, radar, and disdrometer observations for a 27 April 2011 widespread precipitation event. *J. Geophys. Res. Atmos.*, **121**, 5846–5863, https://doi.org/10.1002/2015JD024537.

Grabowski, W. W., 1998: Toward cloud resolving modeling of large-scale tropical circulations: A simple cloud microphysics parameterization. *J. Atmos. Sci.*, **55**, 3283–3298, https://doi.org/10.1175/1520-0469(1998)055<3283:TCRMOL>2.0.CO;2.

Haario, H., E. Saksman, and J. Tamminen, 2001: An adaptive Metropolis algorithm. *Bernoulli*, **7**, 223–242, https://doi.org/10.2307/3318737.

Harrington, J. Y., K. J. Sulia, and H. C. Morrison, 2013a: A method for adaptive habit prediction in bulk microphysical models. Part I: Theoretical development. *J. Atmos. Sci.*, **70**, 349–364, https://doi.org/10.1175/JAS-D-12-040.1.

——, ——, and ——, 2013b: A method for adaptive habit prediction in bulk microphysical models. Part II: Parcel model corroboration. *J. Atmos. Sci.*, **70**, 365–376, https://doi.org/10.1175/JAS-D-12-0152.1.

——, A. Moyle, L. E. Hanson, and H. Morrison, 2019: On calculating deposition coefficients and aspect-ratio evolution in approximate models of ice crystal vapor growth. *J. Atmos. Sci.*, **76**, 1609–1625, https://doi.org/10.1175/JAS-D-18-0319.1.

Hashino, T., and G. J. Tripoli, 2007: The Spectral Ice Habit Prediction System (SHIPS). Part I: Model description and simulation of the vapor deposition process. *J. Atmos. Sci.*, **64**, 2210–2237, https://doi.org/10.1175/JAS3963.1.

Heymsfield, A. J., A. Bansemer, C. Schmitt, C. Twohy, and M. R. Poellot, 2004: Effective ice particle densities derived from aircraft data. *J. Atmos. Sci.*, **61**, 982–1003, https://doi.org/10.1175/1520-0469(2004)061<0982:EIPDDF>2.0.CO;2.

Hindman, E., and D. Johnson, 1972: Numerical simulation of ice particle growth in a cloud of supercooled water droplets. *J. Atmos. Sci.*, **29**, 1313–1321, https://doi.org/10.1175/1520-0469(1972)029<1313:NSOIPG>2.0.CO;2.

Hodyss, D., and N. Nichols, 2015: The error of representation: Basic understanding. *Tellus*, **67A**, 24822, https://doi.org/10.3402/tellusa.v67.24822.

Janjić, T., and S. E. Cohn, 2006: Treatment of observation error due to unresolved scales in atmospheric data assimilation. *Mon. Wea. Rev.*, **134**, 2900–2915, https://doi.org/10.1175/MWR3229.1.

Jensen, A. A., and J. Y. Harrington, 2015: Modeling ice crystal aspect ratio evolution during riming: A single-particle growth model. *J. Atmos. Sci.*, **72**, 2569–2590, https://doi.org/10.1175/JAS-D-14-0297.1.

——, ——, H. Morrison, and J. A. Milbrandt, 2017: Predicting ice shape evolution in a bulk microphysics model. *J. Atmos. Sci.*, **74**, 2081–2104, https://doi.org/10.1175/JAS-D-16-0350.1.

——, ——, and ——, 2018a: Impacts of ice particle shape and density evolution on the distribution of orographic precipitation. *J. Atmos. Sci.*, **75**, 3095–3114, https://doi.org/10.1175/JAS-D-17-0400.1.

——, ——, and ——, 2018b: Microphysical characteristics of squall-line stratiform precipitation and transition zones simulated using an ice particle property-evolving model. *Mon. Wea. Rev.*, **146**, 723–743, https://doi.org/10.1175/MWR-D-17-0215.1.

Kajikawa, M., 1972: Measurement of falling velocity of individual snow crystals. *J. Meteor. Soc. Japan*, **50**, 544–583, https://doi.org/10.2151/jmsj1965.50.6_577.

Kennedy, P. C., and S. A. Rutledge, 2011: S-band dual-polarization radar observations of winter storms. *J. Appl. Meteor. Climatol.*, **50**, 844–858, https://doi.org/10.1175/2010JAMC2558.1.

Kneifel, S., A. von Lerber, J. Tiira, D. Moisseev, P. Kollias, and J. Leinonen, 2015: Observed relations between snowfall microphysics and triple-frequency radar measurements. *J. Geophys. Res. Atmos.*, **120**, 6034–6055, https://doi.org/10.1002/2015JD023156.

Kumjian, M. R., 2013a: Principles and applications of dual-polarization weather radar. Part I: Description of the polarimetric radar variables. *J. Oper. Meteor.*, **1**, 226–242, https://doi.org/10.15191/nwajom.2013.0119.

——, 2013b: Principles and applications of dual-polarization weather radar. Part II: Warm- and cold-season applications. *J. Oper. Meteor.*, **1**, 243–264, https://doi.org/10.15191/nwajom.2013.0120.

——, 2013c: Principles and applications of dual-polarization weather radar. Part III: Artifacts. *J. Oper. Meteor.*, **1**, 265–274, https://doi.org/10.15191/nwajom.2013.0121.

——, and A. V. Ryzhkov, 2010: The impact of evaporation on polarimetric characteristics of rain: Theoretical model and practical implications. *J. Appl. Meteor. Climatol.*, **49**, 1247–1267, https://doi.org/10.1175/2010JAMC2243.1.

——, and ——, 2012: The impact of size sorting on the polarimetric radar variables. *J. Atmos. Sci.*, **69**, 2042–2060, https://doi.org/10.1175/JAS-D-11-0125.1.

——, and O. P. Prat, 2014: The impact of raindrop collisional processes on the polarimetric radar variables. *J. Atmos. Sci.*, **71**, 3052–3067, https://doi.org/10.1175/JAS-D-13-0357.1.

——, and K. A. Lombardo, 2017: Insights into the evolving microphysical and kinematic structure of northeastern U.S. winter storms from dual-polarization Doppler radar. *Mon. Wea. Rev.*, **145**, 1033–1061, https://doi.org/10.1175/MWR-D-15-0451.1.

——, S. A. Rutledge, R. M. Rasmussen, P. C. Kennedy, and M. Dixon, 2014: High-resolution polarimetric radar observations of snow generating cells. *J. Appl. Meteor. Climatol.*, **53**, 1636–1658, https://doi.org/10.1175/JAMC-D-13-0312.1.

——, S. Mishra, S. E. Giangrande, T. Toto, A. V. Ryzhkov, and A. Bansemer, 2016: Polarimetric radar and aircraft observations of saggy bright bands during MC3E. *J. Geophys. Res. Atmos.*, **121**, 3584–3607, https://doi.org/10.1002/2015JD024446.

——, C. Martinkus, O. Prat, S. Collis, M. van Lier-Walqui, and H. Morrison, 2019: A moment-based polarimetric radar forward operator for rain. *J. Appl. Meteor. Climatol.*, **58**, 113–130, https://doi.org/10.1175/JAMC-D-18-0121.1.

Kuo, K., and Coauthors, 2016: The microwave radiative properties of falling snow derived from nonspherical ice particle models. Part I: An extensive database of simulated pristine crystals and aggregate particles, and their scattering properties. *J. Appl. Meteor. Climatol.*, **55**, 691–708, https://doi.org/10.1175/JAMC-D-15-0130.1.

Lamb, D., and W. D. Scott, 1974: The mechanism of ice crystal growth and habit formation. *J. Atmos. Sci.*, **31**, 570–580, https://doi.org/10.1175/1520-0469(1974)031<0570:TMOICG>2.0.CO;2.

Leinonen, J., and D. Moisseev, 2015: What do triple-frequency radar signatures reveal about aggregate snowflakes? *J. Geophys. Res. Atmos.*, **120**, 229–239, https://doi.org/10.1002/2014JD022072.

Libbrecht, K. G., 2003: Growth rates of the principal facets of ice between −10°C and −40°C. *J. Cryst. Growth*, **247**, 530–540, https://doi.org/10.1016/S0022-0248(02)01996-6.

——, 2005: The physics of snow crystals. *Rep. Prog. Phys.*, **68**, 855–895, https://doi.org/10.1088/0034-4885/68/4/R03.

Liljegren, J. C., E. E. Clothiaux, G. G. Mace, S. Kato, and X. Dong, 2001: A new retrieval for cloud liquid water path using ground-based microwave radiometer and measurements of cloud temperature. *J. Geophys. Res.*, **106**, 14 485–14 500, https://doi.org/10.1029/2000JD900817.

Lu, Y., Z. Jiang, K. Aydin, J. Verlinde, E. E. Clothiaux, and G. Botta, 2016: A polarimetric scattering database for nonspherical ice particles at microwave wavelengths. *Atmos. Meas. Tech.*, **9**, 5119–5134, https://doi.org/10.5194/amt-9-5119-2016.

Magono, C., and C. W. Lee, 1966: Meteorological classification of natural snow crystals. *J. Fac. Sci. Hokkaido Univ.*, **2**, 321–335.

Mather, J. H., and J. M. Voyles, 2013: The ARM Climate Research Facility: A review of structure and capabilities. *Bull. Amer. Meteor. Soc.*, **94**, 377–392, https://doi.org/10.1175/BAMS-D-11-00218.1.

Mitchell, D. L., 1996: Use of mass- and area-dimensional power laws for determining precipitation particle terminal velocities. *J. Atmos. Sci.*, **53**, 1710–1723, https://doi.org/10.1175/1520-0469(1996)053<1710:UOMAAD>2.0.CO;2.

Moisseev, D., A. von Lerber, and J. Tirra, 2017: Quantifying the effect of riming on snowfall using ground-based observations. *J. Geophys. Res. Atmos.*, **122**, 4019–4037, https://doi.org/10.1002/2016JD026272.

Morrison, H., and J. A. Milbrandt, 2015: Parameterization of cloud microphysics based on the prediction of bulk ice particle properties. Part I: Scheme description and idealized test. *J. Atmos. Sci.*, **72**, 287–311, https://doi.org/10.1175/JAS-D-14-0065.1.

——, M. van Lier-Walqui, M. R. Kumjian, and O. P. Prat, 2020: A Bayesian approach for statistical-physical bulk parameterization of rain microphysics, Part I: Scheme description. *J. Atmos. Sci.*, **77**, 1019–1041, https://doi.org/10.1175/JAS-D-19-0070.1.

Nelson, J., 2005: Branch growth and sidebranching in snow crystals. *Cryst. Growth Des.*, **5**, 1509–1525, https://doi.org/10.1021/cg049685v.

——, and M. B. Baker, 1996: New theoretical framework for studies of vapor growth and sublimation of small ice crystals in the atmosphere. *J. Geophys. Res.*, **101**, 7033–7047, https://doi.org/10.1029/95JD03162.

Oue, M., M. R. Kumjian, Y. Lu, Z. Jiang, E. Clothiaux, J. Verlinde, and K. Aydin, 2015a: X-band polarimetric and Ka-band Doppler spectral radar observations of a graupel-producing Arctic mixed-phase cloud. *J. Appl. Meteor. Climatol.*, **54**, 1335–1351, https://doi.org/10.1175/JAMC-D-14-0315.1.

——, ——, ——, J. Verlinde, K. Aydin, and E. Clothiaux, 2015b: Linear depolarization ratios of columnar ice crystals in a deep precipitation system over the Arctic observed by zenith-pointing Ka-band Doppler radar. *J. Appl. Meteor. Climatol.*, **54**, 1060–1068, https://doi.org/10.1175/JAMC-D-15-0012.1.

——, M. Galletti, J. Verlinde, A. V. Ryzhkov, and Y. Lu, 2016: Use of X-band differential reflectivity measurements to study shallow Arctic mixed-phase clouds. *J. Appl. Meteor. Climatol.*, **55**, 403–424, https://doi.org/10.1175/JAMC-D-15-0168.1.

Ovchinnikov, M., and Coauthors, 2014: Intercomparison of large-eddy simulations of Arctic mixed-phase clouds: Importance of ice size distribution assumptions. *J. Adv. Model. Earth Syst.*, **6**, 223–248, https://doi.org/10.1002/2013MS000282.

Posselt, D. J., and T. Vukicevic, 2010: Robust characterization of model physics uncertainty for simulations of deep moist convection. *Mon. Wea. Rev.*, **138**, 1513–1535, https://doi.org/10.1175/2009MWR3094.1.

Ryzhkov, A. V., M. Pinsky, A. Pokrovsky, and A. P. Khain, 2011: Polarimetric radar observation operator for a cloud model with spectral microphysics. *J. Appl. Meteor. Climatol.*, **50**, 873–894, https://doi.org/10.1175/2010JAMC2363.1.

——, M. R. Kumjian, S. M. Ganson, and A. P. Khain, 2013: Polarimetric radar characteristics of melting hail. Part I: Theoretical simulations using spectral microphysical modeling. *J. Appl. Meteor. Climatol.*, **52**, 2849–2870, https://doi.org/10.1175/JAMC-D-13-073.1.

Schneebeli, M., N. Dawes, M. Lehning, and A. Berne, 2013: High-resolution vertical profiles of X-band polarimetric radar observables during snowfall in the Swiss Alps. *J. Appl. Meteor. Climatol.*, **52**, 378–394, https://doi.org/10.1175/JAMC-D-12-015.1.

Schrom, R. S., and M. R. Kumjian, 2016: Connecting microphysical processes in Colorado winter storms with vertical profiles of

radar observations. *J. Appl. Meteor. Climatol.*, **55**, 1771–1787, https://doi.org/10.1175/JAMC-D-15-0338.1.

——, and ——, 2018: Bulk-density representations of branched planar ice crystals: Errors in the polarimetric radar variables. *J. Appl. Meteor. Climatol.*, **57**, 333–346, https://doi.org/10.1175/JAMC-D-17-0114.1.

——, and ——, 2019: A probabilistic radar forward model for branched planar ice crystals. *J. Appl. Meteor. Climatol.*, **58**, 1245–1265, https://doi.org/10.1175/JAMC-D-18-0204.1.

——, ——, and Y. Lu, 2015: Polarimetric radar signatures of dendritic growth zones within Colorado winter storms. *J. Appl. Meteor. Climatol.*, **54**, 2365–2388, https://doi.org/10.1175/JAMC-D-15-0004.1.

Sei, T., and T. Gonda, 1989: The growth mechanism and the habit change of ice crystals growing from the vapor phase. *J. Cryst. Growth*, **94**, 697–707, https://doi.org/10.1016/0022-0248(89)90094-8.

Shupe, M. D., P. Kollias, P. Ola, G. Persson, and G. M. McFarquhar, 2008: Vertical motions in Arctic mixed-phase stratiform clouds. *J. Atmos. Sci.*, **65**, 1304–1322, https://doi.org/10.1175/2007JAS2479.1.

Simpfendoerfer, L. F., J. Verlinde, J. Y. Harrington, M. D. Shupe, Y.-S. Chen, E. E. Clothiaux, and J.-C. Golaz, 2019: Formation of Arctic stratocumuli through atmospheric radiative cooling. *J. Geophys. Res. Atmos.*, **124**, 9644–9664, https://doi.org/10.1029/2018JD030189.

Sinclair, V. A., D. Moisseev, and A. von Lerber, 2016: How dual-polarization radar observations can be used to verify model representation of secondary ice. *J. Geophys. Res. Atmos.*, **121**, 10 954–10 970, https://doi.org/10.1002/2016JD025381.

Smolarkiewicz, P. K., 1984: A fully multidimensional positive definite advection transport algorithm with small implicit diffusion. *J. Comput. Phys.*, **54**, 325–362, https://doi.org/10.1016/0021-9991(84)90121-9.

——, and L. G. Margolin, 1998: MPDATA: A finite-difference solver for geophysical flows. *J. Comput. Phys.*, **140**, 459–480, https://doi.org/10.1006/jcph.1998.5901.

Sulia, K. J., J. Y. Harrington, and H. Morrison, 2013: A method for adaptive habit prediction in bulk microphysical models. Part III: Applications and studies within a two-dimensional kinematic model. *J. Atmos. Sci.*, **70**, 3302–3320, https://doi.org/10.1175/JAS-D-12-0316.1.

——, H. Morrison, and J. Y. Harrington, 2014: Dynamical and microphysical evolution during mixed-phase cloud glaciation simulated using the bulk adaptive habit prediction model. *J. Atmos. Sci.*, **71**, 4158–4180, https://doi.org/10.1175/JAS-D-14-0070.1.

Szumowski, M. J., W. W. Grabowski, and H. T. Ochs, 1998: Simple two-dimensional kinematic framework designed to test warm rain microphysical models. *Atmos. Res.*, **45**, 299–326, https://doi.org/10.1016/S0169-8095(97)00082-3.

Takahashi, T., 2014: Influence of liquid water content and temperature on the form and growth of branched planar snow crystals in a cloud. *J. Atmos. Sci.*, **71**, 4127–4142, https://doi.org/10.1175/JAS-D-14-0043.1.

Tang, C., and K. Aydin, 1995: Scattering from ice crystals at 94 and 220 GHz millimeter wave frequencies. *IEEE Trans. Geosci. Remote Sens.*, **33**, 93–99, https://doi.org/10.1109/36.368218.

Todd, C., 1964: A system for computing ice phase hydrometeor development. Meteorology Research Inc. Tech. Rep. ARG-64 Pa-121, 30 pp.

van Lier-Walqui, M., T. Vukicevic, and D. J. Posselt, 2012: Quantification of cloud microphysical parameterization uncertainty using radar reflectivity. *Mon. Wea. Rev.*, **140**, 3442–3466, https://doi.org/10.1175/MWR-D-11-00216.1.

——, H. Morrison, M. R. Kumjian, K. J. Reimel, O. P. Prat, S. Lunderman, and M. Morzfeld, 2020: A Bayesian approach for statistical–physical bulk parameterization of rain microphysics. Part II: Idealized Markov chain Monte Carlo experiments. *J. Atmos. Sci.*, **77**, 1043–1064, https://doi.org/10.1175/JAS-D-19-0071.1.

Vogel, J. M., and F. Fabry, 2018: Contrasting polarimetric observations of stratiform riming and nonriming events. *J. Appl. Meteor. Climatol.*, **57**, 457–476, https://doi.org/10.1175/JAMC-D-16-0370.1.

Yurkin, M. A., and A. G. Hoekstra, 2011: The discrete-dipole-approximation code ADDA: Capabilities and known limitations. *J. Quant. Spectrosc. Rad. Trans.*, **112**, 2234–2247, https://doi.org/10.1016/j.jqsrt.2011.01.031.

Yuter, S. E., and R. A. Houze, 1995: Three-dimensional kinematic and microphysical evolution of Florida cumulonimbus. Part III: Frequency distributions of vertical velocity, reflectivity, and differential reflectivity. *Mon. Wea. Rev.*, **123**, 1941–1963, https://doi.org/10.1175/1520-0493(1995)123<1941:TDKAME>2.0.CO;2.

Zhang, C., and J. Y. Harrington, 2014: Including surface kinetic effects in simple models of ice vapor diffusion. *J. Atmos. Sci.*, **71**, 372–390, https://doi.org/10.1175/JAS-D-13-0103.1.